Alan Dodd Barton

Multipath Tracking and Acoustical Oceanography Measurements in a Stratified Coastal Tidal Channel

(Under the direction of Daniela Di Iorio)

A high-frequency (67 kHz) acoustical scintillation experiment was carried out in the northern entrance to Hood Canal, Puget Sound, WA. This experiment made use of a 4-transmitter and 4-receiver array configured in a T-shape. The two-dimensional feature of this array was designed to measure both along-channel small-scale properties as a result of advection and vertical properties as a result of acoustic refraction from temperature/salinity stratification. With long path lengths and stratified conditions, acoustic propagation resulted in multipath arrivals which were separable for most of the measurement period. A maximum likelihood estimation algorithm is developed that tracks both the direct path signal at approximately 25-30 m depth and the upward refracted signal into the near surface and calculates amplitude, phase, and travel time for each. The acoustical signals are then inverted to estimate along channel flow properties, turbulent effective refractive index levels, and changes in stratification. Along-channel flows exceed 60 cm s^{-1} on strong ebb and the acoustic measurements agree with a tidal model of the currents. Both scalar and vector contributions to the turbulence are analyzed, and show that scalar variability dominates the scattering. The vertical acoustic arrival angle to first order appears to be a sensitive indicator of stratification changes. Finally, analysis of a near surface path shows that surface waves are the dominant contributor to the acoustic amplitude and phase fluctuations and horizontal coherence measurements remain high during a time of weak winds .

Index words: acoustic propagation, tidal channel, Hood Canal Puget Sound

Multipath tracking and acoustical oceanography measurements in a stratified coastal tidal channel

by

Alan Dodd Barton

BIE, Georgia Institute of Technology, 1997

A Thesis Submitted to the Graduate Faculty
of The University of Georgia in Partial Fulfillment
of the
Requirements for the Degree

Master of Science

Athens, Georgia

2002

Multipath tracking and acoustical oceanography measurements in a stratified coastal tidal channel

by

Alan Dodd Barton

Approved:

Major Professor: Daniela Di Iorio

Committee: Jackson O. Blanton
Adrian Burd

Electronic Version Approved:

Gordhan L. Patel
Dean of the Graduate School
The University of Georgia
May 2002

**I dedicate this thesis to my aunt, Ann Barr,
to my parents, Lindsay and Elizabeth Barton,
and to the memory of my grandparents, who
live on in the ravens that watch over my life.**

Acknowledgments

First and foremost, I would like to thank Daniela Di Iorio for allowing me the opportunity to work on a very exciting research project. She has been an excellent mentor, providing the background in acoustic scintillation and ocean physics necessary to complete this experiment, and illustrating the tenacity and attention to detail required for success in this field. I am extremely grateful for all of her support and dedication. I would also like to thank Adrian Burd for his valuable comments and suggestions as a member of my thesis committee, regarding both the content and format of this document. Special thanks are due Jack Blanton, who not only provided excellent insight as a committee member, but also served as an excellent instructor and employer during my summers on Skidaway Island, which provided several memorable field experiences in Georgia's coastal waters.

This research project would not have been possible without the efforts of David Farmer, who supplied this data set for further analysis, and whose scientific contributions with Steven Clifford and Daniela Di Iorio define the theory used for scintillation measurements in Hood Canal. Although I was not present during data collection, I am deeply indebted to Richard Dewey of Science Applications International Corporation (SAIC) and Ward Cartier, Rene Chave, and David Lemon of ASL Environmental Science Ltd. for their efforts in designing and successfully carrying out this experiment, and to Keith Oliver, for thoroughly reporting a preliminary analysis of the data set.

I would like to thank Harold Mofjeld and William Lavelle of the NOAA Pacific Marine Environmental Laboratory, who provided a description of tidal forcings

at the Hood Canal entrance, and Harvey Seim, whose general knowledge of the Puget Sound environment was a valuable resource. I would also like to thank Rich Pawlowicz for personal assistance in utilizing his harmonic analysis package.

I am especially grateful to my friend and colleague Ki Ryong Kang, for his help both in the classroom and out, for the pleasure of knowing him and his family, and for the opportunity to catch a few stingrays together. Thank you to everyone I worked with as a teaching assistant, especially Catherine Teare-Ketter for keeping me gainfully employed, and particularly to Jen, for making it fun, and for always lending an ear to whatever I had to say. Thanks to Trinidad, Cam, and especially Jason for being around when I needed a break. To Matt and Melia, thanks for being so close even though you're far away, and for Carver, who makes me want to be a better person.

Finally, I must say thank you to my family, beginning with my sister Sandra and her husband Michael Vickers, for all their love and concern. I am also extremely grateful to Ann Barr, for being the foundation of our family, and for always encouraging me to continue with my education. To my parents, Lindsay and Elizabeth Barton, thank you for letting me choose my own path, but always being close by with plenty of love and support. Last, but far from least, thank you to Christine Smith, for listening to a thousand practice defenses, for always believing in me, and for helping me find the strength to complete this project.

Table of Contents

List of Figures

List of Tables

Chapter 1

Introduction

Attempts to understand and quantify fluctuations in the refractive index of a medium using acoustic transmissions have received a great deal of attention in recent years, and a few important experiments will be mentioned herein, in terms of their contributions to the growing field of acoustical oceanography. Refractive index fluctuations vary with both space and time, and accumulate along acoustic propagation paths to produce a discernible scintillation pattern on received signals, in terms of amplitude and phase fluctuations. These scintillation patterns were originally examined to understand acoustic propagation in the atmosphere, with concurrent efforts to explain atmospheric scintillation of light (Ishimaru (1978), Chernov (1960), and Tatarskii (1961)). These attempts made initial contributions to the theory of wave propagation through random media (WPRM), which provides the basis for obtaining path-averaged measurements of properties of the intervening medium.

Turbulence is a random process, and must therefore be described in terms of its statistical quantities (Tennekes and Lumley (1999)). The Kolmogorov turbulence model greatly simplifies these statistics within an inertial subrange, through the assumptions of local isotropy and homogeneity. If fluctuations in the medium are assumed isotropic and homogeneous, the Kolmogorov model predicts a $-5/3$ power law spectrum for both vector and scalar fluctuations of the refractive index, and greatly simplifies the inversion of acoustic quantities to understand oceanographic characteristics of the medium.

Traditionally, the study of acoustic fluctuations in oceanic environments has focused on understanding large scale features in the open ocean. Long range tomographic experiments to measure ocean temperature fluctuations, known as Acoustic Thermometry of Ocean Climate (ATOC), have been quite successful (see, for example, the ATOC consortium, Baggeroer et al. (1998)), and are an essential component in understanding global climate change. The nature of open ocean experiments dictates that the smaller scales generally feel the impact of internal waves, which introduces a directional component to the fluctuation patterns and renders the isotropic assumption of the Kolmogorov model invalid. This finding has promoted extensive research in the application of acoustic techniques to study mesoscale internal waves (Munk (1981), Henyey et al. (1986), and Colosi (1996), among others). In addition, most open ocean acoustic experiments feel the effects of multiple scattering, since they are carried out across long distances, through environments that may experience rapid refractive index fluctuations.

In coastal environments, however, strong tidal flows in shallow water often result in fully developed turbulence, which occupies much of the water column, and for which the assumptions of isotropic, homogeneous turbulence may be valid. The work of Farmer and Clifford (1986) made the initial attempt to apply the Kolmogorov model together with Rytov's method of smooth perturbations for weak acoustic scattering to the study of spatial and temporal variability, using a single source and two-receiver horizontal arrays. This represented the first application of acoustic scintillation to study the small scale features of a turbulent tidal channel. The results of this early experiment in a tidal channel were encouraging, and gave the impetus for further application of acoustical scintillation measurement techniques to probe oceanic flows. Application of the Kolmogorov model led to successful path-averaged current measurement in Cordova Channel (Farmer et al. (1987)), an environment characterized by strong tidal flows ($\approx 1 \quad \mathrm{m\,s^{-1}}$) in shallow water

(≈ 30 m). In addition, the experiment showed that scintillation techniques provide a novel method for obtaining path-averaged measurements of turbulent intensity. A key factor contributing to the success of this benchmark experiment was the use of pseudo-random coding to produce a coherent transmission scheme (see Lemon et al. (1987)), which allowed precise measurement of acoustic travel time and amplitude.

Based on the initial success of this experiment, a second experiment was conducted at the same site in Cordova Channel (Di Iorio and Farmer (1994)). This experiment made use of four transmitter, four receiver square arrays for parallel paths, and allowed spatial filtering of received signals (from Farmer and Crawford (1991)). The added dimensions allowed for the first time measurement of horizontal and vertical changes in the acoustic waveform, and direct assessment of anisotropic effects (Di Iorio and Farmer (1996)).

This experiment made several significant contribution to the theory of acoustic scintillation in coastal waters and its application to resolve a number of oceanographic quantities. Independent measurements showed that turbulent velocity fluctuations were the dominant component of acoustical scintillations ($> 90\%$), whereas earlier results had assumed that scalar (temperature) fluctuations contributed most to the scintillation pattern. Based on this result, a novel path averaged measure of turbulent kinetic energy dissipation was obtained from the acoustic data. Further analysis of the data (Di Iorio and Farmer (1996)) used the two-dimensional acoustic arrays to measure horizontal and vertical arrival angles, which give insight into the degree of anisotropy present in the turbulent environment. Vertical arrival angle measurements were also inverted to supply a novel measurement of the path averaged sound speed gradient with depth. This entire body of work showed the effectiveness of scintillation techniques in probing coastal oceanic environments, and set the stage for the Hood Canal Acoustic Propagation Experiment, which is the subject of this analysis.

1.1 Motivation

The study of turbulence in coastal environments has many practical applications, both to the scientific community and the general public. Hood Canal represents one of the most pristine environments in Puget Sound, as the pressures of human encroachment are thus far less severe than in neighboring tidal channels. Low population density and limited river runoff contribute to healthy eelgrass meadows, and large seasonal algal blooms supply a food source for a number of marine species (Gustafson et al. (2000)). Improved characterization of the turbulent environment will assist in prediction of these algal blooms, and their impacts on the abundant zooplankton species found in this environment. The impacts are transferable to higher trophic levels, including a large number of commercially important marine species such as the Pacific Hake, Cod, and Walleye Pollock (from Gustafson et al. (2000)), which find safe haven and abundant food sources in the healthy eelgrass meadows of Hood Canal.

Although Hood Canal is less polluted than other coastal fjords within Puget Sound (from Gustafson et al. (2000)), a better understanding of the turbulent environment is transferable to similar environments more dramatically influenced by human population, and indeed to coastal tidal channels around the world. Most transport calculations to estimate mixing and flushing rates in these coastal fjords have made use of traditional moorings, which are generally local in character, and may not be representative of mean conditions across the canal width. Other methods employ towed instrumentation (for example, Fleury and Lueck (1992)) or vertical profilers (including Alford et al. (1999)) to obtain spatial resolution of turbulent parameters and mean flows, but are limited to short time scales by high operational costs. Acoustical scintillation systems circumvent both of these major obstacles, first by providing path averaged measures of mean and turbulent quantities, which

are generally very good representations of mean conditions across the canal width. Once in place, scintillation systems can remain in operation for extended periods, and provide a continuous record of properties of the intervening medium. These results can provide insight into slowly evolving variability across long time scales, and contribute significantly to our understanding of the temporal evolution of path averaged turbulence and mean flows in coastal tidal channels.

1.2 Experimental Approach

The Hood Canal Acoustic Propagation Experiment was conducted from October 19-23, 1993, just inside the canal entrance off Admiralty Inlet. The site was chosen to test the limitations of a 67 kHz acoustical scintillation system in a long range environment characterized by strong tidal flows and vertical stratification. The path length (2380 m) far exceeds previous applications of acoustic scintillation in coastal tidal channels, which were limited to a range of 670 m. The two-dimensional transmitter and receiver arrays were constructed from the existing instrumentation used in Cordova Channel (Di Iorio and Farmer (1994)), and the 67 kHz carrier frequency was not the ideal choice for this very long range (2380 m path length) environment. The received acoustic signals were characterized by multipath arrivals, and as a result, implementation of a method to accurately measure and separate these multipath signals is an important component of this analysis. Di Iorio and Farmer (1993) developed a maximum likelihood algorithm to simultaneously track three closely spaced acoustic arrivals in a quiescent fjord, and the proper parameterization of this algorithm for use in this environment is implemented.

The two arrivals of interest are a fairly direct path connecting transmitter to receiver and a near surface path, which at times shows a single reflection off the sea surface. Independent measurements allow the application of ray theory to deter-

mine the path traveled by each signal, as a result of refraction from the intervening medium. This information, along with the successful implementation of the two path tracking algorithm, resolves precise measurements of amplitude, phase, and relative arrival time for each path, and comparison of log-amplitude, phase, and phase difference spectra show agreement with the Kolmogorov model for isotropic and homogeneous turbulence together with the weak scattering theory.

Efforts to accomplish the inverse problem of resolving oceanographic measurements from the received signals focus on the direct acoustic path. Path averaged measurements of along channel current are successfully derived, and are compared with independent current meter measurements and existing tidal models. The acoustic current speeds correspond more directly with modeled currents, illustrating the advantage of path averaged measurements over point measurements for transport estimation in tidal channels.

The direct path signal also provides a measure of turbulent intensity, in terms of the effective refractive index structure parameter. Independent measurements from a fast sampling current meter and conductivity-temperature-depth (CTD) time series provide insight into the relative vector and scalar contributions to turbulent intensity, respectively. Results show that scalar variability dominates the turbulence in Hood Canal, a result quite different from that observed in Cordova Channel (Di Iorio and Farmer (1994)). From the fast sampling current meter, vector contributions to the turbulence are also expressed in terms of the dissipation rate of turbulent kinetic energy ϵ. Similarly, the scalar component of turbulent intensity is expressed in terms of the dissipation rate of sound speed variance ϵ_c, a parameter that is dominated by temperature variability.

The measured vertical arrival angle of the direct path signal gives a path averaged estimate of the sound speed gradient with depth. Comparison with independent measurements does not show similar trends, since the independent measurement is

essentially local in character. From CTD data, a mean temperature/salinity relationship is determined, and the acoustic sound speed is inverted to give a path averaged measure of relative changes in stratification, in terms of the buoyancy frequency $(N^2)'$ about an arbitrary mean.

Preliminary work with the near surface acoustic path shows the influence of the surface wave field, and acoustic scintillations were dominated by surface waves and/or orbital motions. Analysis of a short time series shows high spatial coherence between horizontally spaced receivers, a surprising result for such large receiver separations and a long path length. Further analysis is left as an interesting avenue for future work.

1.3 Thesis Outline

A summary of the background theory applied directly in this environment is presented in Chapter 2. This includes a number of statistical definitions and a brief treatment of the theory of weak scattering of acoustic signals, as well a description of the Kolmogorov model for isotropic, homogeneous turbulence.

Chapter 3 describes the experimental setup, and defines the dimensions of the T-shaped transducer arrays. The physical orientation of the arrays across the Hood Canal entrance is explained, along with the relative positions of the current meter mooring and meteorological station. This chapter also presents a number of acoustic parameters, and describes the coherent scheme of acoustic transmissions.

The forward problem of successfully resolving the received acoustic signals is discussed in Chapter 4. This includes an explanation of ray path prediction, and relates this information to the time series of acoustic amplitude and arrival time. The maximum likelihood algorithm used to track and separate the two acoustic arrivals is described, including a detailed treatment of the mathematical development of Di

Iorio and Farmer (1993). Finally, the parameterization required for implementation in this long range environment is shown, and results are compared with the Kolmogorov model with weak scattering.

Chapter 5 tackles the inverse problem of resolving useful oceanographic measurements from the acoustic signals. Path averaged measurements of current are obtained, and are compared with current meters and an existing tidal model. Also, acoustic vertical arrival angle measurements give a path averaged estimate of changes in stratification. The dissipation rate of turbulent kinetic energy is measured from a fast sampling current meter, and a parameter representing the dissipation rate of sound speed variance is obtained from CTD time series. These results are then converted to show their individual contributions to the acoustic structure parameter measurement of the effective refractive index fluctuations. Finally, an initial investigation of the near surface acoustic path shows that the acoustic scintillations are dominated by surface waves and that high coherence exists between horizontally spaced receivers.

Chapter 6 gives the conclusions of the thesis, and summarizes the oceanographic measurements obtained in this analysis. Some suggestions for future work are also given.

Chapter 2

Theory

Understanding acoustic scintillation patterns in a turbulent environment requires an understanding of the existing theory of wave propagation through moving random media (WPRM). Acoustic scintillations are produced by random irregularities in the medium, which accumulate across the path of acoustic propagation to alter the amplitude and phase of the signal. Assuming fully-developed turbulence together with weak acoustic scattering makes it possible to gain information about the intervening medium and resolve some valuable oceanographic measurements from the inversion of the received acoustic signals.

2.1 Kolmogorov Model

The foundations for this approach lie in the classical results of Kolmogorov, who defined the inertial subrange of scales over which the simplifying assumptions of isotropic, homogeneous turbulence may be applied. Tennekes and Lumley (1999) showed that for flows with sufficiently high Reynolds number

$$\mathrm{Re} = \frac{U\ell}{\nu} \,, \tag{2.1}$$

where $\nu = 1 \times 10^{-6} \mathrm{m}^2\ \mathrm{s}^{-1}$ is the kinematic viscosity, U is the mean flow, and ℓ is a characteristic length scale, there exists a range of scales over which local isotropy can be assumed. The largest, energy containing scales are by definition anisotropic and therefore set the upper limit, or outer scale (L_0), of the inertial subrange. This

outer scale for stratified flows could be characterized by the Ozmidov length scale $L_O = (\epsilon/N^3)^{1/2}$ (see Stacey (1999)), where ϵ is the dissipation rate of turbulent kinetic energy per unit mass and $N^2 = (-g/\rho_0)(\partial\sigma_T/\partial z)$ is the buoyancy frequency (from Pond and Pickard (1983)).

In the inertial subrange, energy is received from large scales and cascades to smaller and smaller scales. At some small scale, velocity gradients become large enough that viscous dissipation of energy and diffusion of scalar variability become most important. This scale size defines the lower limit of the inertial subrange, and is defined as the inner scale (l_0) of the turbulence.

In this context, turbulence refers to turbulent effective refractive index fluctuations, which include contributions from velocity fluctuations as well as fluctuations of passive scalar quantities such as temperature and salinity (see Di Iorio and Farmer (1994)). The theoretical work of Tatarskii (1971) and Ostachev (1994) (or, alternatively, Ostachev (1997)) defines the three-dimensional spectrum for the effective refractive index fluctuations as

$$\Phi_{n_{\text{eff}}}(K) = \frac{\Phi_c(K)}{c_0^2} + \frac{n_j n_k \Phi_{jk}(K)}{c_0^2}, \tag{2.2}$$

$$= \frac{\Phi_c(K)}{c_0^2} + \frac{n_j n_k}{c_0^2}\left[\frac{E(K)}{4\pi K^2}\left(\delta_{jk} - \frac{K_j K_k}{K^2}\right)\right], \tag{2.3}$$

where $\Phi_c(K)$ is the three dimensional wavenumber (K) spectrum of sound speed fluctuations, $\Phi_{jk}(K)$ is the three dimensional wavenumber spectrum for velocity fluctuations, $E(K)$ is the three dimensional energy spectrum for $\frac{2\pi}{L_0} \ll K \ll \frac{2\pi}{\ell_0}$, c_0^2 is a mean sound speed, δ_{jk} is the Kronecker function, and n_j is the unit vector aligned in the direction of acoustic scatter. These equations assume zero correlation between vector and scalar fluctuations.

In the inertial subrange, Tennekes and Lumley (1999) define

$$E(K) = 1.5\epsilon^{2/3}K^{-5/3}, \tag{2.4}$$

where the constant 1.5 is an empirical Kolmogorov constant, and $1/2 < u_i^2 > \; = \int_0^\infty E(K)dK$. The three dimensional energy spectrum can also be expressed as

$$\frac{E(K)}{4\pi K^2} = 0.033 \left(\frac{11}{6} C_v^2\right) K^{-11/3}, \tag{2.5}$$

where

$$C_v^2 = 1.97\epsilon^{2/3}, \tag{2.6}$$

relates the level of turbulent velocity fluctuations C_v^2 to the dissipation rate of turbulent kinetic energy ϵ, and C_v^2 is called the structure parameter for velocity.

The three-dimensional Kolmogorov spectrum for sound speed fluctuations is

$$\Phi_c(K) = 0.033 C_c^2 K^{-11/3} \; , \tag{2.7}$$

where C_c^2 is the structure parameter for sound speed and is a measure of the level of sound speed fluctuations. The three dimensional spectrum of sound speed variance (from Shaw et al. (2001), adapted from the scalar variance spectrum described in Tennekes and Lumley (1999)) is

$$E_c(K) = 0.79\epsilon_c\epsilon^{-1/3}K^{-5/3} \; , \tag{2.8}$$

where 0.79 is an empirical Kolmogorov constant, ϵ_c is the dissipation rate of sound speed variance, $1/2 < c^2 > \; = \int_0^\infty E_c(K)dK$, and where

$$C_c^2 = 3.82\epsilon_c\epsilon^{-1/3}. \tag{2.9}$$

The above results give the three-dimensional statistics for velocity and scalar fluctuations. In most cases, however, measurements are limited to one-dimensional spectral statistics. Hinze (1959) showed that the one-dimensional spectrum for velocity fluctuations aligned in the direction of mean flow is,

$$F_{11}(K_1) = \int_{K_2} \int_{K_3} \Phi_{11}(\mathbf{K}) \, dK_2 \, dK_3, \tag{2.10}$$

and aligned perpendicular to the mean flow,

$$F_{22}(K_1) = \int_{K_2} \int_{K_3} \Phi_{22}(\mathbf{K})\, dK_2\, dK_3. \tag{2.11}$$

Applying the result obtained in (2.4) for the energy spectrum E(K) in an inertial subrange, Hinze (1959) derives the one-dimensional spectrum as

$$\begin{aligned} F_{11}(K_1) &= \frac{9}{55} 1.5 \epsilon^{2/3} K_1^{-5/3}\ , & (2.12)\\ F_{22}(K_1) &= \frac{4}{3} F_{11}(K_1) \\ &= \frac{4}{3}\frac{9}{55} 1.5 \epsilon^{2/3} K_1^{-5/3}\ , & (2.13) \end{aligned}$$

where the variance $1/2 < u^2 > \ = \int_0^\infty F_{11}(K_1)\, dK_1$ and $1/2 < v^2 > \ = \int_0^\infty F_{22}(K_1)\, dK_1$.

Hinze (1959) shows the one-dimensional spectrum for scalar fluctuations and Shaw et al. (2001) gives the one-dimensional spectrum for sound speed fluctuations, yielding

$$\begin{aligned} F_c(K_1) &= \int_{K_2} \int_{K_3} \Phi_c(\mathbf{K})\, dK_2\, dK_3\ , & (2.14)\\ &= 0.124 C_c^2 K_1^{-5/3}\ , & (2.15)\\ &= \frac{3}{5}\, 0.79 \epsilon_c \epsilon^{-1/3} K_1^{-5/3}, & (2.16) \end{aligned}$$

where the assumption of isotropic and homogeneous turbulence in the inertial subrange applies.

Substituting (2.5) and (2.7) into (2.3) and assuming zero scattering angle for forward scattered waves yields

$$\begin{aligned} \Phi_{\eta_{\text{eff}}} &= 0.033 \left(C_{\eta_s}^2 + \frac{11}{6} C_{\eta_v}^2 \right) K^{-11/3}, & (2.17)\\ &= 0.033 C_{\eta_{\text{eff}}}^2 K^{-11/3} & (2.18) \end{aligned}$$

where $C_{\eta_s} = C_c^2/c_o^2$, $C_{\eta_v}^2 = C_v^2/c_o^2$, and the final result makes the substitution for the total effective structure parameter $C_{\eta_{\text{eff}}}^2$, defined by Ostachev (1994) as

$$C_{\eta_{\text{eff}}}^2 = C_{\eta_s}^2 + \frac{11}{6} C_{\eta_v}^2\ . \tag{2.19}$$

2.2 Weak Scattering Theory

The Helmholtz equation for the sound pressure $p(\mathbf{r}) = A(\mathbf{r})e^{iS(\mathbf{r})}$ in a moving medium simplified by Di Iorio and Farmer (1996) is

$$\nabla^2 p(\mathbf{r}) + k^2 n(\mathbf{r})^2 p(\mathbf{r}) = -2ikn^2(\mathbf{r})\frac{\mathbf{u}\cdot\nabla p(\mathbf{r})}{c_0}, \tag{2.20}$$

where k is the acoustic wavenumber and $n(\mathbf{r}) = \frac{c_0}{c(\mathbf{r})}$ is the refractive index of the medium due to sound speed changes from scalars. For small gradients of log amplitude and phase fluctuations ($\nabla\chi$ and $\nabla\phi << 1$), Tatarskii (1971) applied Rytov's method of smooth perturbations, which solves the Helmholtz equation for $\Psi = \ln p = \Psi_0 + \Psi_1$, and $n = n_0 + n'$, yielding the first order equation for weak scattering of acoustic signals

$$\nabla^2\Psi_1 + 2\nabla\Psi_0\cdot\nabla\Psi_1 = -2\eta_{\text{eff}}k^2, \tag{2.21}$$

where $\Psi_1 = \ln p_1 = \ln\frac{A}{A_0} + i(S - S_0) = \chi + i\phi$, and χ and ϕ represent the log-amplitude and phase fluctuations of the received signal, respectively, and (A_0, S_0) are the amplitude and phase for wave propagation in a medium with no refractive index variations or mean flow. The effective refractive index fluctuations,

$$\eta_{\text{eff}} = \frac{-c' - \mathbf{u}\cdot\hat{n}}{c_0}\,, \tag{2.22}$$

are influenced by scalar refractive index fluctuations and the component of velocity in the direction of acoustic propagation.

2.3 Statistical Functions

2.3.1 Covariance functions

Clifford and Farmer (1983) applied the time-lagged covariance function for log-amplitude χ fluctuations, measured over a horizontal array assuming isotropy and

homogeneity,

$$C_\chi(r,\tau) = < [\chi(r_1,t) - < \chi(r_1,t) >][\chi(r_1+r,t+\tau) - < \chi(r_1+r,t+\tau) >] > \quad . \quad (2.23)$$

If the turbulent structure can be considered a statistically 'frozen field' over the time scale required to pass through the acoustic array, then the Taylor hypothesis can be applied, which transforms temporal fluctuations to spatial ones via $K = \frac{2\pi f}{U}$.

The scale sizes of importance for amplitude fluctuations are those sizes that can focus or defocus the acoustic signal, defined by the Fresnel scale $(\lambda L)^{1/2}$, where λ is the acoustic wavelength and L is the path length. If these scale sizes fall within the inertial subrange of isotropic, homogeneous turbulence in the plane perpendicular to acoustic propagation, the wave number $\mathbf{K} = (K_x, 0, K_z)$ can be integrated over spherical coordinates, and the resulting covariance function assuming spherically spreading waves is,

$$C_\chi(r,\tau) = 4\pi^2 k^2 \int_0^L dy \int_0^\infty dK K \Phi_{n_{\text{eff}}}(K) \sin^2\left(\frac{K^2 y(L-y)}{2kL}\right) J_0(KA(r,\tau)), \quad (2.24)$$

which is described as an integral along the path $0 \leq y \leq L$, and over all refractive index wavenumbers $K = (K_x^2 + K_z^2)^{1/2}$, where k is the acoustic wavenumber and J_0 is a zero-order Bessel function. Di Iorio and Farmer (1996) have shown that the Bessel function in (2.24) is a function of receiver spacing, where

$$A(r,\tau) = \begin{cases} |\frac{r_x y}{L} - U\tau| & \text{horizontally spaced receivers,} \\ \sqrt{(\frac{r_z y}{L})^2 + (U\tau)^2} & \text{vertically spaced receivers,} \end{cases} \quad (2.25)$$

and U is the component of velocity in the direction parallel to the transducer separation r_x. In this definition, acoustic propagation is from a single transmitter to two receivers, resulting in diverging paths. For parallel paths (two transmitters, two receivers),

$$A(r,\tau) = \begin{cases} |r_x - U\tau| & \text{horizontally spaced receivers,} \\ \sqrt{r_z^2 + (U\tau)^2} & \text{vertically spaced receivers.} \end{cases} \quad (2.26)$$

For $r = 0$ and $\tau = 0$, (2.24) represents the log amplitude variance of the signal, and is defined as

$$C_\chi(0,0) = \sigma_\chi^2 = 0.124 k^{7/6} L^{11/6} C_{n_{\text{eff}}}^2 \ . \tag{2.27}$$

The amplitude fluctuations are sensitive to the Fresnel scale size $\sqrt{\lambda L}$, whereas phase variability is sensitive to the largest scales, because it is a measure of travel time across the full width of the canal. These large scales cannot be considered homogeneous, and introduce large scale temporal variability into the phase measurement. As a result, the phase difference ($[\delta\phi(r,t) = \phi(r_1,t) - \phi(r_1+r,t)]$) is often used, which essentially acts as a high pass filter, where ϕ is a zero mean process as defined previously (following Equation (2.21)). The auto covariance of the phase difference function excludes large scale inhomogeneities shared by the two phase measurements, and was derived by Di Iorio and Farmer (1996) for horizontally and vertically spaced receivers as

$$\begin{aligned} R_{\delta\phi}(\tau) &= < \delta\phi(r,t)\delta\phi(r,t+\tau) > & (2.28)\\ &= 2R_\phi(\tau) - C_\phi(r,\tau) - C_\phi(-r,\tau) & (2.29)\\ &= 4\pi^2 k^2 \int_0^L dy \int_0^\infty dK K \Phi_{n_{\text{eff}}}(K) \cos^2\left(\frac{K^2 y(L-y)}{2kL}\right) \\ &\quad \times [2J_0(KU\tau) - J_0(KA(r,\tau)) - J_0(KA(-r,\tau))]. & (2.30) \end{aligned}$$

2.3.2 Structure functions

In the study of turbulence, the structure function for a random variable is often utilized, and essentially acts as a high pass filter to remove large scale inhomogeneities. The wave structure function for spherically spreading waves is defined as

$$D(r,\tau) = < (\chi(r_1,t) - \chi(r_1+r,t+\tau))^2 > + < (\phi(r_1,t) - \phi(r_1+r,t+\tau))^2 > , \tag{2.31}$$

and includes contributions from both log-amplitude and phase, respectively, but is mostly dominated by the phase difference variability. Theoretically, Farmer et al.

(1987) defined it as,

$$D(r,\tau) = 8\pi^2 k^2 \int_0^L dy \int_0^\infty dK K \Phi_{n_{\text{eff}}}(K)(1 - J_0(KA(r,\tau))) \ . \tag{2.32}$$

For $\tau = 0$, (2.32) approximates the phase difference variance,

$$D(r,\tau=0) \approx D_\phi(r,\tau=0) =< \delta\phi^2 >= 1.09 k^2 L C^2_{\eta_{\text{eff}}} r^{5/3} \ \text{(diverging paths)} \tag{2.33}$$

$$D(r,\tau=0) \approx D_\phi(r,\tau=0) =< \delta\phi^2 >= 2.91 k^2 L C^2_{\eta_{\text{eff}}} r^{5/3} \ \text{(parallel paths)} \ . \tag{2.34}$$

2.4 Spectral Functions

Clifford (1971) derived the temporal power spectra for the log-amplitude and phase as

$$W^\phi_\chi(f) = 8\pi^2 k^2 U^{-1} \int_0^L \int_{K_0}^\infty dK \frac{K\Phi_{n_{\text{eff}}}(K)}{(K^2 - K_0^2)^{1/2}} \begin{matrix}\cos^2 \\ \sin^2\end{matrix} \left(\frac{K^2 y(L-y)}{2kL}\right) \ , \tag{2.35}$$

where $K_0 = \frac{2\pi f}{U}$ is the minimum refractive index wavenumber. Normalizing each spectra by the log-amplitude variance $\sigma^2_\chi = 2\int_0^\infty W_\chi(f)\, df$ (defined in (2.27)) allows comparison between measured spectra of χ and ϕ power spectral densities, when plotted as a function of frequency f.

Similarly, Clifford (1971) derived the form of the temporal power spectrum for the phase difference for horizontally spaced receivers (diverging paths) as,

$$\begin{aligned} W_{\delta\phi_x}(f) = \ & 32\pi^2 k^2 U^{-1} \int_0^L dy \int_{K_0}^\infty dK \frac{K\Phi_{n_{\text{eff}}}(K)}{(K^2 - K_0^2)^{1/2}} \\ & \times \sin^2\left(K_0 \frac{r_x y}{2L}\right) \cos^2\left(\frac{K^2 y(L-y)}{2kL}\right), \end{aligned} \tag{2.36}$$

and Di Iorio and Farmer (1996) for vertically spaced receivers (diverging paths) as,

$$\begin{aligned} W_{\delta\phi_z}(f) = \ & 32\pi^2 k^2 U^{-1} \int_0^L dy \int_{K_0}^\infty dK \frac{K\Phi_{n_{\text{eff}}}(K)}{(K^2 - K_0^2)^{1/2}} \\ & \times \sin^2\left((K^2 - K_0^2)^{1/2} \frac{r_z y}{2L}\right) \cos^2\left(\frac{K^2 y(L-y)}{2kL}\right). \end{aligned} \tag{2.37}$$

In this case, the normalization is the phase difference variance $< \delta\phi^2 >= 2 \int_0^\infty W_{\delta\phi}(f)\, df$ defined in (2.33). The result allows comparison to measured phase difference spectra, when plotted as a function of frequency f.

These theoretical power spectra for the log amplitude χ, phase ϕ, and phase differences $\delta\phi_x$ and $\delta\phi_z$ will be compared with the measured spectra in Hood Canal to determine the validity of the assumptions of isotropic, homogeneous turbulence with weak scattering.

Chapter 3

Experimental Setup

The Hood Canal Acoustic Propagation Experiment was carried out from October 19-23, 1993 by Science Applications International Corporation (SAIC) of Bellevue, Washington, in collaboration with the Acoustical Oceanography Research Group at the Institute of Ocean Sciences of Sidney, British Columbia. Technical support for the acoustical scintillation instrumentation was supplied by ASL Environmental Sciences of Sidney, British Columbia.

3.1 Acoustical Measurements

Acoustic data were collected from transmitter and receiver arrays located at the Northern entrance to Hood Canal, Puget Sound, Washington (see Figure 3.1). This location was selected because Hood Canal is fairly deep, with maximum depths approximately 100 meters, and is characterized by relatively strong tidal flows with moderate vertical stratification. The canal entrance is 2380 meters wide, which represents a fairly long range for a 67 kHz acoustical propagation experiment. This combination of factors make the area of particular interest in extending the acoustical scintillation measurement technique to general coastal conditions.

The transmitter array was bottom-mounted on the western side of the canal entrance, at a depth of 21.5 meters. The receiver array was mounted at a depth of 26.5 meters on the eastern bank, and was oriented such that the direction of acoustic propagation was roughly perpendicular to the direction of mean flow through the

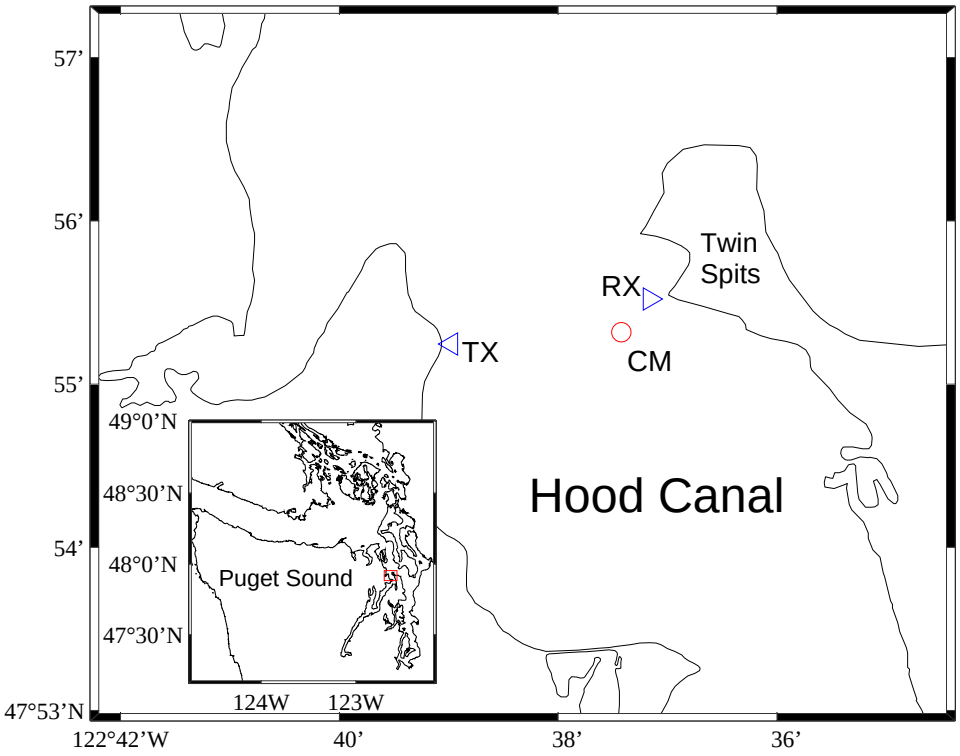

Figure 3.1: Map of Puget Sound, Washington and the northern entrance to Hood Canal, showing locations of the transmitter array (TX), receiver array (RX), and current meter (CM) mooring.

channel (see Figure 3.1). Each array consisted of four transducers oriented in a T-shape, with dimensions and orientation as shown in Figure 3.2, to allow for both horizontal and vertical resolution of acoustic variability introduced by the medium. Each transmitter communicates with each of the four receivers, giving a total of 16 channels of information. Table 3.1 lists the assignment of a channel number to each transmitter-receiver combination. Maximum separation between transducers was 3.07 meters in the horizontal, and the center transducer was slightly offset toward the northernmost end of the array. This arrangement provided three different aperture lengths across which turbulent eddies may be advected. The fourth transducer was

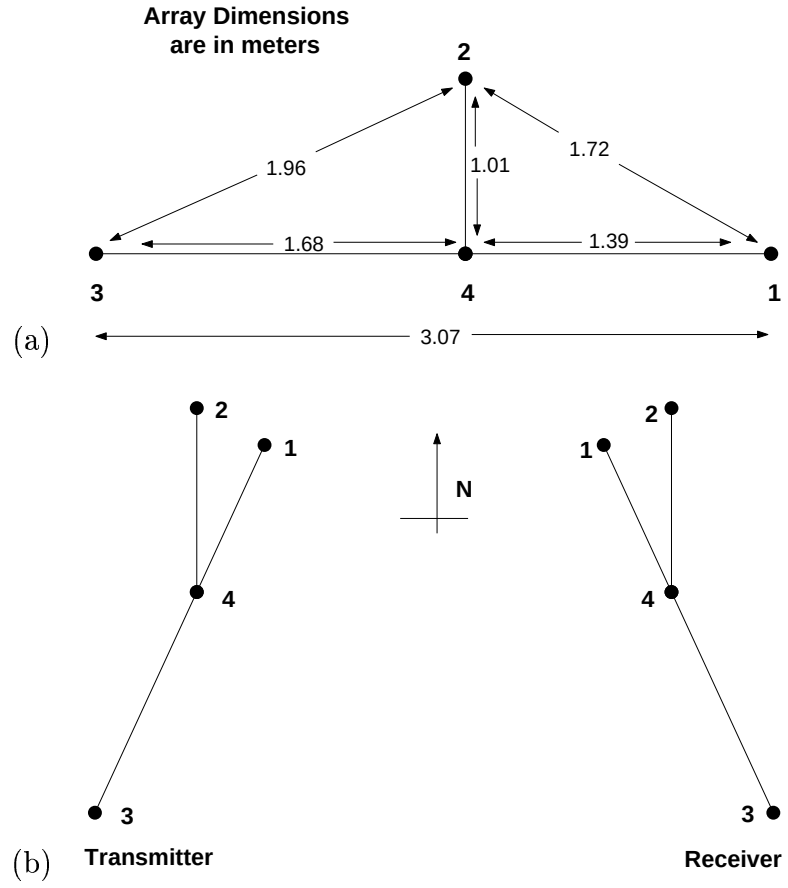

Figure 3.2: (a) Transmitter and receiver array dimensions and (b) their orientation across the canal.

Table 3.1: Channel Designations for each transmitter (T) and receiver (R) combination.

	R1	R2	R3	R4
T1	1	2	3	4
T2	5	6	7	8
T3	9	10	11	12
T4	13	14	15	16

Table 3.2: Acoustic Parameters

Transmitter Depth (m)	21.5
Receiver Depth (m)	26.5
Path Length L (m)	2380
Average Sound Speed ($\mathrm{m\,s^{-1}}$)	1489
Acoustic Frequency (Hz)	67567
Acoustic Wavenumber k ($\mathrm{m^{-1}}$)	287.82
Fresnel Scale $\sqrt{\lambda L}$ (m)	7.2081
Code Length (bits (ms))	127 (17)
Bit Width (cycles/bit (μs)	9 (133)
Phase Shift for Coding (deg)	180
Digitization Rate (samples/bit (kHz))	3 (22.5)
Window Size (samples (ms))	121 (5.37)
Repetition Rate (Hz)	5.0
Observation Period	19/10/93 10:32 to 20/10/93 19:26
(Year Day)	(292.4 to 293.8)

displaced upward by 1.01 meters to better understand vertical variability within the Hood Canal environment.

Table 3.2 summarizes the acoustic experimental parameters used in this experiment. Transmissions were 180-degree phase modulated and encoded using pseudo-random noise (PRN) m-sequences to improve the signal to noise ratio and provide a more precise phase measurement (see Lemon et al. (1987)). Signals were sent in the form of 127 bit PRN code from successive transmitters at a cycle repetition (ping) rate of 5 Hz. Each bit corresponds to 9 cycles of the acoustic carrier frequency of $f = 67567$ Hz, making the total code length 16.9 ms and the bit width 133μs.

Received signals were multiplied by $\cos \omega t$ and $\sin \omega t$ ($\omega = 2\pi f$ is the angular acoustic frequency), thus converting to in-phase ($I(t)$) and quadrature ($Q(t)$) components, respectively. Signals were then low pass filtered to remove the 67567 Hz

carrier frequency, reducing the signals to baseband. They were then digitized at 3 samples/bit and correlated with a template of the transmitted PRN code. Each transmitter/receiver combination consists of in-phase and quadrature components, as a function of arrival time for each transmission. The amplitude is then defined as

$$A(t) = \sqrt{I(t)^2 + Q(t)^2}, \tag{3.1}$$

and the phase as

$$\phi(t) = \arctan\left(\frac{Q(t)}{I(t)}\right), \tag{3.2}$$

where t represents the arrival time. The phase represents fractional cycles of the transmission and can be used as a more accurate travel time estimate when added to an integer number of complete cycles required to traverse the canal (obtained from the mean arrival time). A large arrival time window of 5.37 ms (121 samples) was used for each transmitter-receiver combination to ensure that all multipath arrivals were recorded.

Transmissions were in block mode to provide a clear time separation between the end of T4 and the beginning of T1 transmission. Each block of code consisted of a cycle of transmissions through all four sources in the order $T1_1$, T1, T2, T3, T4, $T4_2$. Transmissions ($T1_1$,T2), (T1,T3), (T2,T4), (T3,$T4_2$) acted as guard sequences for T1, T2, T3, and T4, respectively, so as to further improve the signal to noise ratio (SNR) by reducing correlation side lobe noise from the received signals (see Lemon et al. (1987)). For the remainder of this discussion, a single ping of information is defined as a cycle containing one transmission from each of the four sources in the order T1, T2, T3, T4. The signal from each of the four sources was detected almost simultaneously at each of the four receivers, resulting in a total of sixteen channels of information from a single ping of the array, as listed in Table 3.1.

The time series of acoustic data began at approximately 10:30 AM on October 19, 1993 (Year Day 292.4375), and data collection continued until 7:27 PM the

following day, October 20. During the experiment, data acquisition was interrupted occasionally to back up recorded data or to service the generators that powered the system. Therefore, some gaps exist within the acoustic time series, but for the most part, the study yielded a fairly continuous time series spanning more than two repetitions of the tidal cycle within the thirty-three hour experimental period. This represents a robust data set for further analysis.

3.2 Environmental Data

In addition to the acoustic data collected during the experiment, a number of independent measurements were made to facilitate understanding of the physical environment at the Hood Canal entrance. These were recorded with a meteorological station, three moored current meters, several conductivity-temperature-depth (CTD) measurements, and a pair of Seabird Microcats moored on the western and eastern sides of the canal entrance at 11 and 5 meters depth, respectively.

The meteorological sensors were stationed on the eastern shore of the canal entrance to provide measurements of wind speed and direction at 10 meters above the surface. The weather station was positioned at Twin Spits, very near the receiver mooring, and should therefore provide an accurate representation of wind effects over the path of acoustic propagation.

A vertical array of current meters was moored near the eastern edge of the Hood Canal entrance, approximately 500 meters from the receiving transducers and just outside the path of acoustic propagation (as shown in Figure 3.1). Current meter data collection began at 5:30 PM on October 18, one day prior to the start of the acoustic experiment, and continued until 9:00 AM on October 21, after the completion of the acoustic experiment. Therefore, an uninterrupted time series of data was available for comparison with the acoustic results. The current meter

mooring was comprised of three instruments. Two Aanderaa current meters were moored at 20 m at 40 m depth and sampled continuously at a sampling rate of 0.0167 Hz (once per minute) throughout the duration of the experiment. The third current meter on the mooring was an S4 burst sampling current meter (BSCM), which was suspended at 30 m depth. Once per hour, the BSCM collected a two minute burst of data at a sampling rate of 2 Hz. The faster sampling rate allowed calculation of power spectral densities (PSDs) for each burst of data.

The majority of conductivity-temperature-depth (CTD) data were collected from short casts, and will be used to predict the ray paths connecting transmitter to receiver. Eight of these casts were collected near the center of Hood Canal, close to the path of acoustic propagation. The remaining five were collected in rapid succession during a transect across the width of the canal. In addition to the casts, two short (23 minute) time series of CTD data (sampling at 2 Hz) were also collected on the second day of the experiment. These measurements were collected at both 12 m and 30 m depth, and are used for PSD estimation of scalar variance levels.

Pressure sensors were moored on either bank at the canal entrance, and recorded one sample per minute for the duration of the experiment. Both sensors were Seabird Microcat instruments measuring temperature, conductivity, and pressure. Conductivity and pressure measurements were converted internally to salinity and depth, respectively. Water depth at the eastern bank instrument ranged from 2.5-6 meters, while the instrument on the western bank was slightly deeper, at depths ranging from 9-12.5 meters.

Chapter 4

Two path separation algorithm

4.1 Motivation

The complete time series of acoustic data for Channel 1 (T1 to R1) windowed on the first two arrivals is shown in Figure 4.1, and displays the amplitude of the dominant signals as a function of arrival time and elapsed time. Also shown is the along channel current speed at 20 m depth, with arrows denoting the times of CTD profiles. The acoustic data shows that a single transmission results in two persistent arrivals at a given receiver: a direct path through the center of the water column at approximately 25 m depth, and a downward refracted path that may interact with the sea surface, as will be discussed.

To describe this result requires an understanding of the intervening medium's effects on the propagation of these 67 kHz transmissions. Sound propagates along spherically spreading wave fronts and, in the Hood Canal experiment, the transducers were restricted with a 10 degree conical beamwidth. In the horizontal, these spreading phase fronts may be influenced by along-channel advective processes. The direction of vertical propagation is influenced by refraction due to temperature/salinity stratification, which may or may not include reflection off the surface or bottom. Therefore, a single transmission may result in multiple arrivals at a given receiver. Since Hood Canal is a tidally forced flow with stratification, this data set provides an opportunity to first successfully track the arrivals, and then to gain some insight into both the acoustical and oceanographic variability within the system at

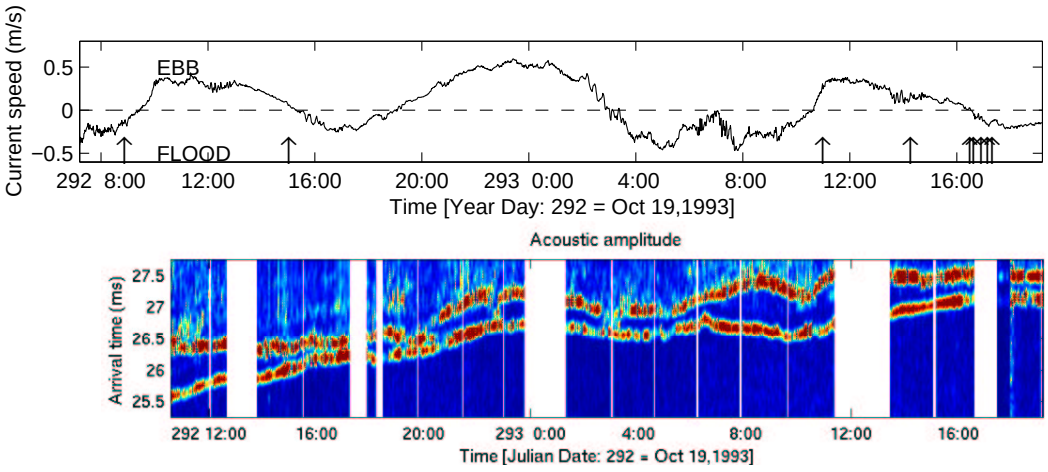

Figure 4.1: Along channel current measurements at 20 m depth, with arrows denoting the times of CTD profiles, and the complete time series of acoustic data showing amplitude as a function of arrival time and as a function of elapsed time.

the depth of the acoustic path. The independent CTD measurements labeled in Figure 4.1 (arrows) are used to predict the acoustic paths resulting in these closely spaced arrivals.

4.1.1 Ray tracing and CTD measurements

The majority of CTD data were collected during the acoustic measurements and provide vertical profiles of the mean refractive index, which dictate the ray paths that connect transmitter to receiver. The arrival time along the ray is dictated by soundspeed (which is dominated by temperature) and the component of flow in the direction of the ray path. The large scale trend of increasing arrival time shown in Figure 4.1 across the 33 hour experimental period, however, is more likely the result of experimental clock drift, since no corresponding trend is observed in the

environmental (temperature and cross channel current) data, which will be shown in Figure 5.2.

In this experiment, the acoustic rays are restricted to a 10° beamwidth launched between ±5° from the transmitter. As an acoustic signal traverses the width of the canal, the wavefront spreads through the water column. The wavefronts are the surfaces normal to the acoustic rays radiating away from the transmitter. Changes in the refractive index profile of the medium will redirect each ray, according to Snell's law of refraction (see Brekhovskikh and Lysanov (1982)), defined as

$$c_1 \cos\theta_1 = c_2 \cos\theta_2,$$

where c_i is the sound speed of the ith layer and the angle θ_i is defined from the vertical axis. At times, the mean refractive index ($n(r) = \frac{c_0}{c(r)}$) decreases enough at the surface to produce ray paths that are wholly refracted and never reach the sea surface. Lower refractive index values at the surface denote an increase in sound speed, and Snell's law dictates that the angle of refraction (with the vertical) will increase. As a result, the ray is refracted downward in the direction of lower sound speed (higher refractive index).

When the mean refractive index changes slowly with depth, the angle of refraction will be smaller, and the ray will reflect off the sea surface (or bottom). Since the refractive index of the medium is dictated by its temperature, salinity, and pressure, CTD data allows for prediction of the ray paths that will connect transmitter to receiver in Hood Canal. These paths are called eigenrays.

Ray tracing diagrams were generated using existing software developed by Bowlin (1994), and are shown in Figure 4.2. Four of the nine CTD casts were collected near the center of the channel, with all but one falling within the window of acoustic data collection. In Figure 4.1(a), arrows on the current graphs show the time at

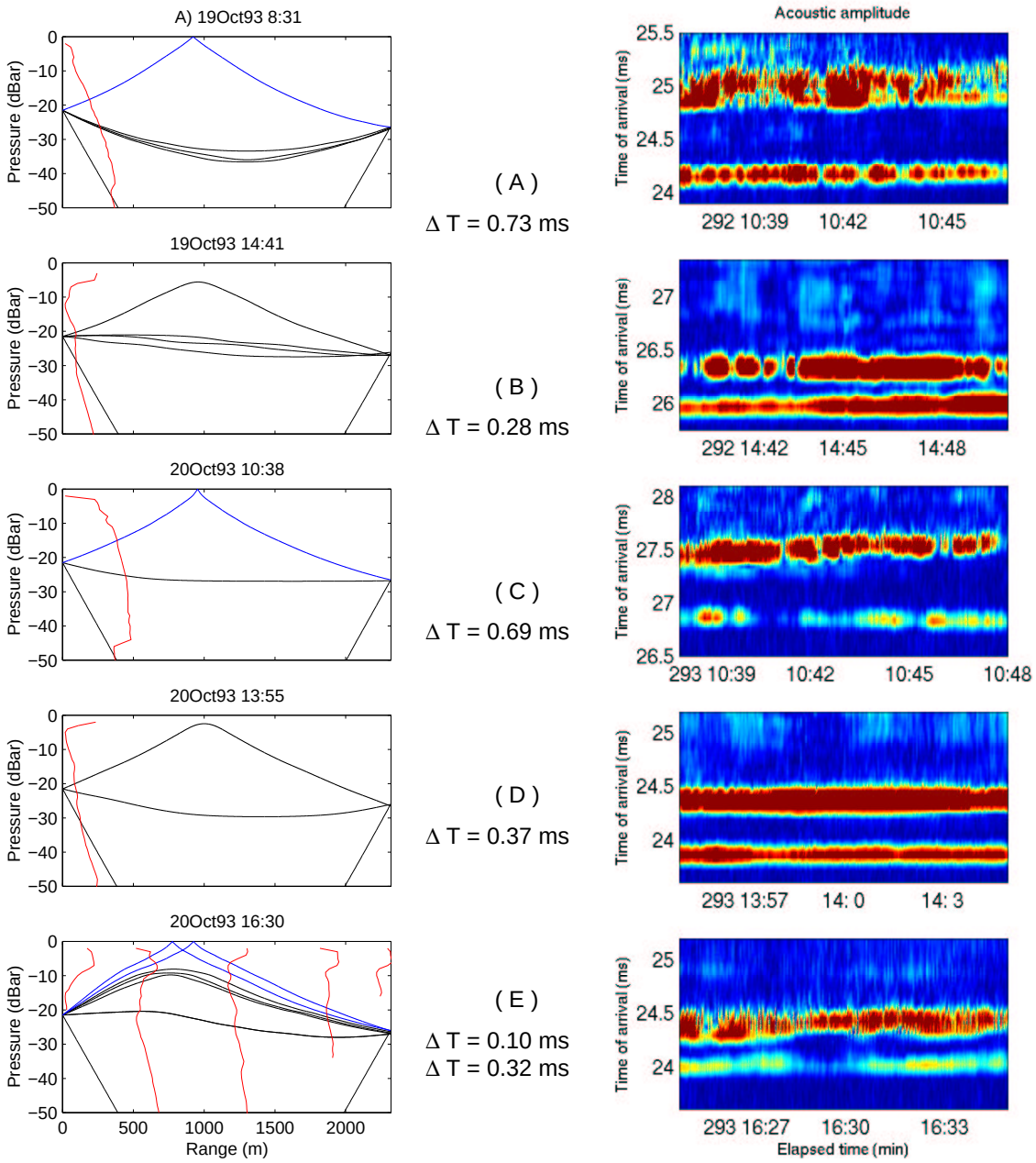

Figure 4.2: Ray tracing diagrams constructed from CTD data (red), with wholly refracted paths shown in black and surface reflected in blue, along with corresponding sections of the acoustic time series, windowed on the most direct path and near surface or surface reflected path. Values of ΔT signify the travel time separation between the direct first arrival and the second arrival predicted from the ray tracing.

which each CTD profile was collected and provide an opportunity to understand the relationship between the tidal cycle and changes in stratification within the system.

Using each of these individual casts, four range independent ray tracing diagrams were generated based on the assumption of a horizontally uniform sound speed field. These are displayed in Figure 4.2(a-d), and predict a direct path, a near surface path, and a bottom-reflected path, all connecting transmitter to receiver. To the right of each ray diagram, short time series of acoustic amplitude versus elapsed time and time of arrival are shown, windowed on the time that each CTD profile was recorded. The acoustic arrivals shown are also windowed on the two closely spaced signals, the direct path and the near surface path. The bottom-reflected signal travels a much longer path length, and therefore arrives much later, resulting in a very weak signal. At all times, the bottom-reflected signal is well separated from the two signals of interest, and has therefore been omitted from the figure. In all four cases (in Figure 4.2a-d), the travel time differences, shown on the figure as ΔT, predicted by the ray tracing algorithm provided a fairly accurate representation of the travel time differences seen in the acoustic data.

Of the remaining CTD profiles, five were collected in rapid succession in a transect across the width of the canal entrance as the tide started to flood. Arrows in Figure 4.1 again denote the times at which the profiles were collected. Together, they provided a range-dependent profile of temperature and salinity variations for use in predicting the acoustic ray paths connecting transmitter to receiver. When supplied with the range-dependent information from the five casts, the software returned a complex set of 7 eigenrays connecting transmitter to receiver, as shown in Figure 4.2(e). Many of these signals have very little time separation and hence arrive simultaneously. The first of these arrivals is predicted to travel a fairly direct route through the center of the water column to the receiver. Ray tracing predicts a $\Delta T = 0.1$ ms between this most direct path and the near surface wholly refracted

path, and a $\Delta T = 0.3$ ms between the direct path and the surface reflected paths. The acoustic data plotted on the right side of Figure 4.2(e) shows two persistent arrivals, with the first arriving approximately 0.3 ms before the second, which represent the direct and surface reflected paths. The wholly refracted signal is not visible in the acoustic time series, but the direct path signal is weak and intermittent as a result of defocusing and possible multiple scattering effects.

Examining the five diagrams as a group provides an understanding of ray path evolution with time. Changes in sound speed dictate that the direct path is sometimes refracted to depths below 30 m, but generally traverses the channel at approximately 22 m depth. The near surface path is more variable, since sound speed is dominated by the temperature variability, with cooler waters having low sound speed and warmer temperatures producing higher sound speed. Following ebb events, warmer surface waters are advected through Hood Canal and into the path of acoustic propagation. As a result, the transmission accelerates in the near surface waters and is refracted downward in the direction of lower sound speed, as dictated by Snell's Law. Temporal separation between the two arrivals is small, and the near surface path is wholly refracted, as shown in Figure 4.2(b & d).

Following strong flood events (see Figure 4.2(a) & (c)), elevated surface water temperatures are absent, presumably the result of advection of oceanic water masses. As a result, the upward refracted signal reflects off the sea surface before reaching the receiver. Since the transmission slows down in the near surface waters and travels a slightly longer path length, this surface-reflected signal arrives considerably later than the direct path arrival. The two arrivals are well separated, and ray tracing models predict time of arrival differences of approximately 0.7 ms. A near surface Microcat temperature time series shown in Figure 4.3 supports the variations of temperature with tidal cycle, and shows warm surface waters during the end of ebb events and cooler surface water during the end of flood.

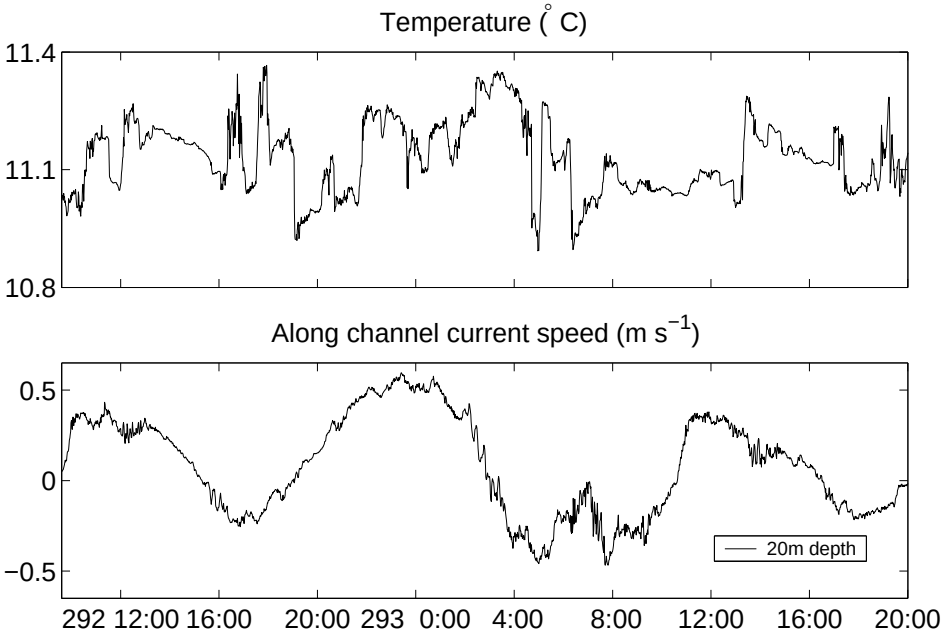

Figure 4.3: Temperature from the western moored Microcat at 9 m depth through the tidal cycle.

The surface reflected signal would typically show much temporal spreading and large, high frequency amplitude variability, indicative of the surface scattering process (see Bjerrum-Niese (1998)), which can be seen in Figure 4.2(a) & (c), and is also evident in the range-dependent diagram shown in Figure 4.2(e). Through analysis of a short segment of data during a surface reflection phase, but when temporal spreading is minimal, we will attempt to understand its interaction with the surface wave field, as will be discussed in Section 5.3.2.

These ray tracing diagrams assign depths to the two acoustic measurements, and provide the essential link between the acoustics and the physical environment of Hood Canal. They show that sound speed variability in Hood Canal results in two main acoustic ray paths that are sometimes well-separated in time (by as much

as 0.73 ms), but later arrive with small temporal separation. In addition, refractive index variability produces several less persistent micropaths that complicate the set of received signals. This characteristic provides the motivation to develop an algorithm to simultaneously isolate and track two paths, to obtain amplitude, phase, and travel time fluctuations for these signals, while at the same time windowing on the data to exclude other multipath arrivals.

4.2 Mathematical development

To separate these closely spaced multipaths, a maximum likelihood estimation algorithm was implemented following the work of Ehrenberg et al. (1978). The mathematical model of the received signal *r(t)* is

$$r(t) = \sum_{i=1}^{N} A_i s(t - \tau_i) + n(t) \tag{4.1}$$

where A_i and τ_i are the amplitude and arrival times for the ith path of a total of N paths, t is the elapsed arrival time, and $n(t)$ represents noise. The signal s(t) is the theoretical result obtained by Menemenlis and Farmer (1992), which is obtained by applying an impulse response function (which simulates the reduction to base band of the received signal) to the theoretical PRN correlation function. It is defined by

$$s(t - \tau) = \sum_{n=0}^{9} a_n \left(\frac{t - \tau}{\tau_p} \right)^{2n} , \tag{4.2}$$

where a_n are known coefficients and $\tau_p = 1$ bit is the half-width of the correlation peak. In this experiment, the half-width of the correlation peak is 3 samples, since each bit represents 9 cycles of the 67567 Hz carrier and the digitization rate is three samples per bit. With a half-width of 3 samples, a window of seven samples centered on the peak is required to isolate the entire peak.

The maximum likelihood estimation algorithm derived by Di Iorio and Farmer (1993) minimizes the function,

$$\begin{aligned} Q &= \sum_t \left[r(t) - \sum_{i=1}^{N} A_i s(t-\tau_i) \right]^2 \\ &= \sum_t r(t)^2 - 2 \left[\sum_{j=1}^{N} A_j C(\tau_j) - \frac{1}{2} \sum_{j=1}^{N} A_j \sum_{k=1}^{N} A_k B(\tau_j, \tau_k) \right] \end{aligned} \tag{4.3}$$

with respect to A_i and τ_i. Here,

$$B(\tau_j, \tau_k) = \sum_t s(t-\tau_j) s(t-\tau_k) \tag{4.4}$$

represents the auto correlation between modeled signals, and

$$C(\tau_j) = \sum_t r(t) s(t-\tau_j) \tag{4.5}$$

represents the cross correlation between the received and modeled signals. To minimize Q in (4.3), the last term on the right hand side of the equation must be maximized. In matrix form, this can be represented as,

$$\text{maximize} \quad C^T A - \frac{1}{2} A^T B A \quad \text{w.r.t.} \ A_i \ \text{and} \ \tau_i, \tag{4.6}$$

where A, B, and C are defined as,

$$A^T = [A_1, A_2, \cdots, A_N], \tag{4.7}$$

$$C^T = [C(\tau_1), C(\tau_2), \cdots, C(\tau_N)], \tag{4.8}$$

$$B = \begin{bmatrix} B(\tau_1,\tau_1) & B(\tau_1,\tau_2) & \cdots & B(\tau_1,\tau_N) \\ B(\tau_2,\tau_1) & B(\tau_2,\tau_2) & \cdots & B(\tau_2,\tau_N) \\ \vdots & \vdots & \vdots & \vdots \\ B(\tau_N,\tau_1) & B(\tau_N,\tau_1) & \cdots & B(\tau_N,\tau_N) \end{bmatrix}. \tag{4.9}$$

If (4.6) is maximized w.r.t. each of the A_i, the result is

$$A = B^{-1} C. \tag{4.10}$$

Finally, substituting (4.10) into (4.6) yields the maximization problem

$$\begin{aligned} \text{maximize} \quad & \tfrac{1}{2} C^T B^{-1} C \quad \text{w.r.t. } \tau_i, \\ \text{or minimize} \quad & -\tfrac{1}{2} C^T B^{-1} C \quad \text{w.r.t. } \tau_i. \end{aligned} \tag{4.11}$$

Plugging the result of this minimization into (4.10) gives an amplitude A_i for each of the ith paths. Linear interpolation of the phase measurements from (3.2) at the travel time estimates gives a more accurate measurement of the travel time.

4.3 Implementation in Hood Canal

In Hood Canal, the two closely spaced multipaths representing the direct and near surface eigenrays are of interest. Therefore, this algorithm was implemented for $N = 2$ paths. Initially, the user supplies two arrival times for each channel from a graph of the raw amplitude and phase information (refer to Figure 4.4). Instead of performing the maximization over the entire window of 121 samples, the user also supplies a window width wide enough to record both multipath arrivals. The algorithm then centers this window on the two arrivals, using the average of the two initial time of arrival estimates. By isolating this smaller section of the arrival window, interference from less stable micropaths is minimized.

Using the user-supplied arrival times as a starting point, the minimization presented in (4.11) is carried out using a constrained sequential quadratic programming method (described by Press et al. (1992)), with the following constraints,

$$\begin{aligned} \tau_2 &\geq \tau_1 + 2.67 \text{ samples} , \\ \text{lb} \leq \tau_1 &\leq \text{ub} , \\ \text{and} \qquad \text{lb} \leq \tau_2 &\leq \text{ub} , \end{aligned} \tag{4.12}$$

where ub and lb are the upper and lower bounds, respectively, determined from the initial, user-defined window position.

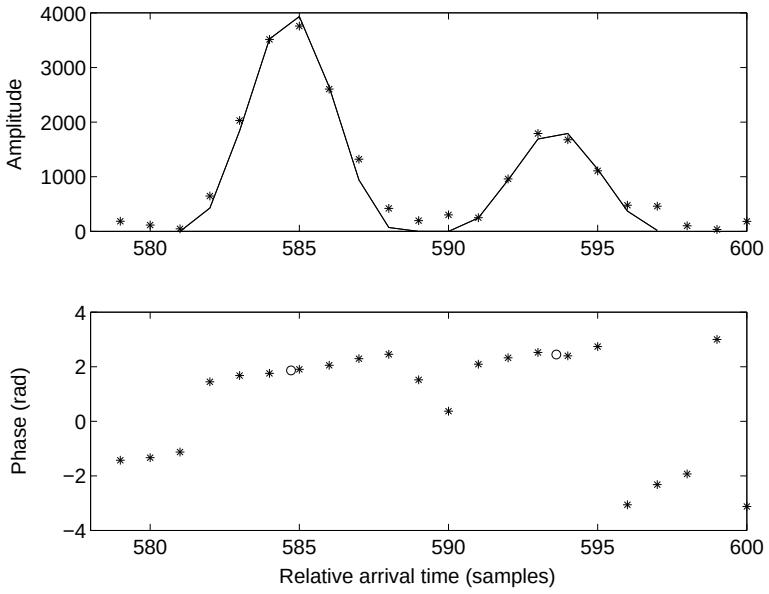

Figure 4.4: Amplitude and phase (*) as a function of arrival time for a single transmission, along with the corresponding modeled signal (solid line) and linearly interpolated phase (o). The peak locations give an amplitude, arrival time, and phase for each path.

In addition to the constraint imposed by the window boundaries, the minimization of (4.11) is subject to the first constraint defined in (4.12), which dictates that the two peaks can be no closer to one another than 2.67 samples (8 cycles). The half width (τ_p) of a single peak is three samples, and clear separation of two multipaths is 2 bits (6 samples=18 cycles). Since the theoretical shape of the received signal is known, the constraint is reduced to 2.67 samples, pushing the limitations of the algorithm to resolve the two individual peak locations. This constraint is also required to prevent the algorithm from fitting both τ_1 and τ_2 under a single arrival when the second arrival is weak or absent. Instead, the value of τ_2 is forced 2.67 samples away, and fits to noise when the second arrival is absent.

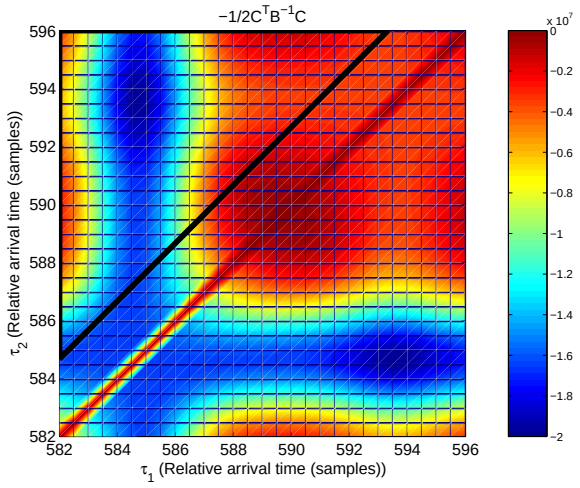

Figure 4.5: Evaluation of $-\frac{1}{2}C^T B^{-1} C$ by a constrained sequential quadratic programming method returns a single minimum at $\tau_1 = 584.8$ and $\tau_2 = 593.7$ samples. The minimization is carried out in the black triangle, which represents the constraints $\tau_2 \geq \tau_1 + 2.67$, $\text{lb} \leq \tau_1 \leq \text{ub}$, and $\text{lb} \leq \tau_2 \leq \text{ub}$, where ub and lb represent the upper and lower bounds set by the user-defined window.

Under these constraints, and with an initial guess for arrival time, the algorithm quickly converges to a solution for τ_1 and τ_2. Figure 4.5 shows results for a single ping, and shows a clear minimum to the function in (4.11) at values of $\tau_1 = 584.8$ samples and $\tau_2 = 593.7$ samples. The minimization is carried out within the black triangle, which is defined by the constraints in (4.12). Figure 4.5 also shows local maxima along the diagonal line corresponding to $\tau_1 = \tau_2$. At all values of $\tau_1 = \tau_2$, the inverse (B^{-1}) of the auto-correlation defined in (4.9) goes to infinity, and the function $-1/2\ C^T B^{-1} C$ is arbitrarily set to 1×10^5. Since the function is symmetric about this diagonal line, τ_1 and τ_2 could be swapped if the first constraint in (4.12) were omitted.

From these time of arrival estimates, amplitude (A) is calculated using (4.10). The solid curve in Figure 4.4 shows the result of the minimization, and the result fits closely to the data (*). Equation (3.2) gives the phase measurement for each sample (as shown in Figure 4.4 as *), and the phase for the received signal is obtained by linear interpolation at the optimized arrival time τ_1 and τ_2. Figure 4.4 shows that phase is nearly constant during the arrival of the first signal, and the phase at $\tau_1 = 584.8$ can be interpolated linearly between the phase measurements for sample 584 and 585. Similarly, the phase remains fairly constant during the second arrival, and the phase measurement at $\tau_2 = 593.7$ is interpolated between samples 593 and 594. These refined arrival time measurements replace the user-defined peak locations and provide more precise travel times for the first ping of information.

The refined values of τ_1 and τ_2 for the first ping become the initialization for the second ping of information. The algorithm proceeds through all the data in this manner, using the previous pings' arrival time estimates as a starting point for the minimization for each subsequent ping. In most cases, the arrival time for a given path τ_i should not vary greatly from ping to ping. Therefore, some error checking is implemented to ensure that values of τ_i do not vary by more than 0.67 samples (2 cycles) from the previous ping. If this restriction is violated, the algorithm simply keeps the arrival time recorded on the previous ping. However, variability in Hood Canal dictates that sudden changes in arrival time of this magnitude are not uncommon, due to fade outs of both the direct and near surface acoustic signals. To account for this, the algorithm tests the stability of the new arrival. If the change in arrival time exceeds 0.67 samples for eight consecutive pings, then the change in arrival time is assumed to be stable, and the algorithm accepts the new arrival time estimate.

Larger scale variations in the acoustic data also influence the performance of the two path tracking algorithm. The data is divided into segments that are generally

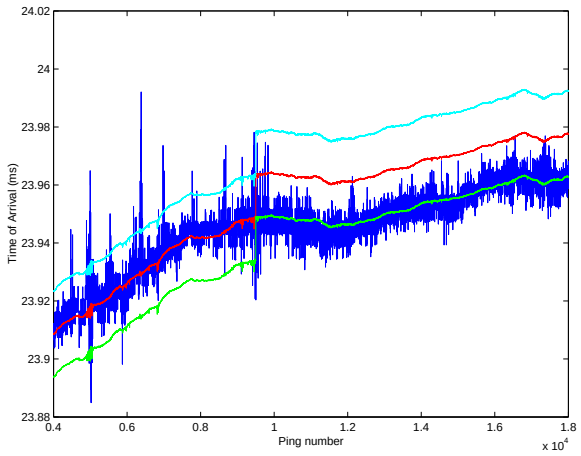

Figure 4.6: Short time series of time of arrival (blue), overlaid with phase (red). An offset representing an integer number of 2π cycles has been added to the phase values to line up with time of arrival. The cyan and green curves represent phase plus or minus one cycle, respectively, and clearly show the 360 degree phase jump at ping 9500.

1-1.5 hours in length. During this time, variability in Hood Canal can produce large changes in the mean arrival times of each signal. As a result, the arrivals may drift outside the user-defined window position set on the first ping. To compensate, the window position remains fixed for the first 1000 pings, but then is allowed to move. The algorithm calculates an average arrival time for each path from the previous 1000 pings (3.33 minutes), then centers the window on the two values. The moving window allows the algorithm to adjust to large scale changes in the mean refractive index and remain centered on the two arrivals of interest. Although its position changes, the window width remains fixed at its original value, and a properly selected window width allows the window to move and track the two main arrivals while excluding unstable micropaths at the edges of the window.

Time of arrival estimates are used to resolve 360° ambiguities in the phase measurement, as is shown in Figure 4.6. If the acoustic transmission is thought of as a sinusoidal wave, the mean arrival time in cycles represents a number of complete cycles of the signal, whereas the phase represents fractions of a cycle. A time offset representing the integral number of elapsed complete cycles is added to the phase measurement, so that time of arrival can be compared directly with phase. Since the phase of the signal is nearly constant at the time of arrival (refer to Figure 4.4), it can be used to refine the time of arrival estimate, since its accuracy is fractions of a cycle. However, the nature of the arctan function in (3.2) for the phase calculation introduces phase wrap around, and unwrapping the phase can result in 360° (2π) phase jumps when there is a noisy measurement. Although the time of arrival is a noisier signal, it's general shape should mirror that of the phase measurement when the ray paths are well defined. Sudden changes in phase denote 360° (2π) jumps, which are corrected to provide a better fit to the time of arrival. The time series shown in Figure 4.6 illustrates this point. The sudden change in phase at ping 9500 is a 2π jump, which is manually corrected before analysis of the final output. Correcting these ambiguities aligns the phase measurement with the noisy arrival time estimates, and supplies a time series of precise travel time measurements.

It should be noted that the recorded travel time measurements are relative to the receiver ping timing mark and not the transmitter timing mark. Therefore, these arrival time measurements do not represent the time required to traverse the channel. It is the relative fluctuations that are of interest.

Implementation of the two path tracking algorithm was carried out on the complete acoustic time series, and the refined amplitude, phase, and time of arrival measurements were recorded. During post-processing of the phase to remove 360° (2π) jumps, amplitude measurements were converted to log-amplitude ($\chi = \ln A / < A >$) to give the final output. The resulting phase and log-amplitude time series can then

be compared with theory to test and validate the assumptions of isotropic, homogeneous turbulence and weak scattering in Hood Canal.

4.4 COMPARISON WITH THEORY

The theoretical spectra for the log-amplitude, phase, and phase difference defined in section 2.4 are valid in an inertial subrange where isotropy and homogeneity can be applied together with weak acoustic scattering. The assumption of weak scattering requires that the log amplitude variance σ_χ^2 (defined in (2.27)) be $\ll 0.25$ (see Tatarskii (1971)), and Figure 4.7 shows the complete time series of σ_χ^2 during the experimental period. The diamond ($\diamond$) at Year Day 293 14:29 denotes a time when $\sigma_\chi^2 \ll 0.25$, and the square ($\square$) at Year Day 293 4:42 denotes a time when $\sigma_\chi^2 \approx 0.25$, at which time the assumption of weak scattering may break down. These two times represent the extremes of log amplitude variability, and are used for comparison with the theoretical spectra for log-amplitude χ and phase ϕ (both defined by (2.35)), horizontal phase difference $\delta\phi_x$ (defined in (2.36)), and vertical phase difference $\delta\phi_z$ (defined in (2.37)).

Before calculation of the four power spectral densities (PSDs) from the data, and before further analysis, each parameter was low-pass filtered to reduce contamination from high frequency noise. A third order Butterworth filter was implemented, and data were forward and reverse filtered to produce zero phase distortion. The low pass cutoff frequency used changed with the tidal cycle. Strong tidal flows produced more energetic high frequency fluctuations, so the low pass cutoff frequency is higher than during times of slack water.

From the filtered data, PSDs for the log-amplitude, phase, and both horizontal and vertical phase difference were generated. PSDs were obtained from individual 1-1.5 hour data files by generating overlapping segments of 8192 data points with

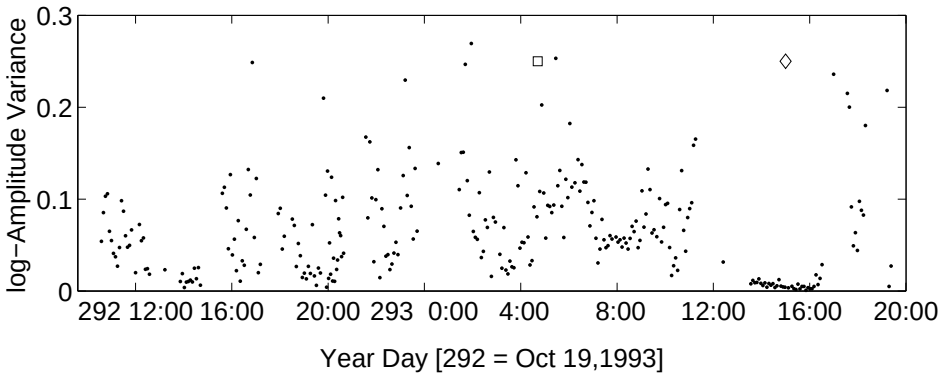

Figure 4.7: A complete time series of the log amplitude variance for a single channel. The diamond ($\diamond$) is a time when $\sigma_\chi^2 \ll 0.25$, and the square ($\square$) is a time when $\sigma_\chi^2 \approx 0.25$

a Hanning window, fast Fourier transforming, and averaging over all segments to obtain the average spectrum for each of the four parameters. The resulting log-amplitude and phase spectra are normalized by the log-amplitude variance σ_χ^2 before comparison with the theoretical spectra. The log-amplitude variance is the proper normalization for phase spectra, since the phase variance is subject to large scale variability, and is thus difficult to measure accurately.

The horizontal phase difference for diverging paths was calculated using the maximum horizontal separation between receivers ($r_x = 3.07$ m) to focus on scales near the Fresnel radius ($\sqrt{\lambda\ell} = 7.28$ m), and the vertical phase difference was calculated across the $r_z = 1.01$ m vertical separation between receivers. The normalization for each spectrum is the phase difference variance for diverging paths $< \delta\phi^2 > \approx D(r, 0)$, where $D(r, 0)$ is the wave structure function (defined by 2.33) at $\tau = 0$.

The normalized spectra corresponding to the diamond ($\diamond$) in Figure 4.7 are displayed in Figure 4.8, along with the theoretical spectra, and represent a time when

$\sigma_\chi^2 \ll 0.25$, at approximately slack water. The results in all four spectra show good agreement at the high frequencies with the Kolmogorov model for isotropic, homogeneous turbulence with weak scattering. The theoretical log-amplitude (χ) spectrum peaks at $f_0 = \frac{U}{\sqrt{\lambda \ell}} \approx 0.02Hz$ $(\log f_0 = -1.7)$, and the measured spectrum shows increased levels from larger scale structures.

Similarly, the normalized spectra corresponding to the square ($\square$) in Figure 4.7 are displayed in Figure 4.9 during strong flow, and again show close agreement with the theoretical spectra. This is a surprising result, since $\sigma_\chi^2 \approx 0.25$ at this time and the flow is approaching maximum flood, and validates the application of the Kolmogorov model together with weak scattering across the duration of the experiment.

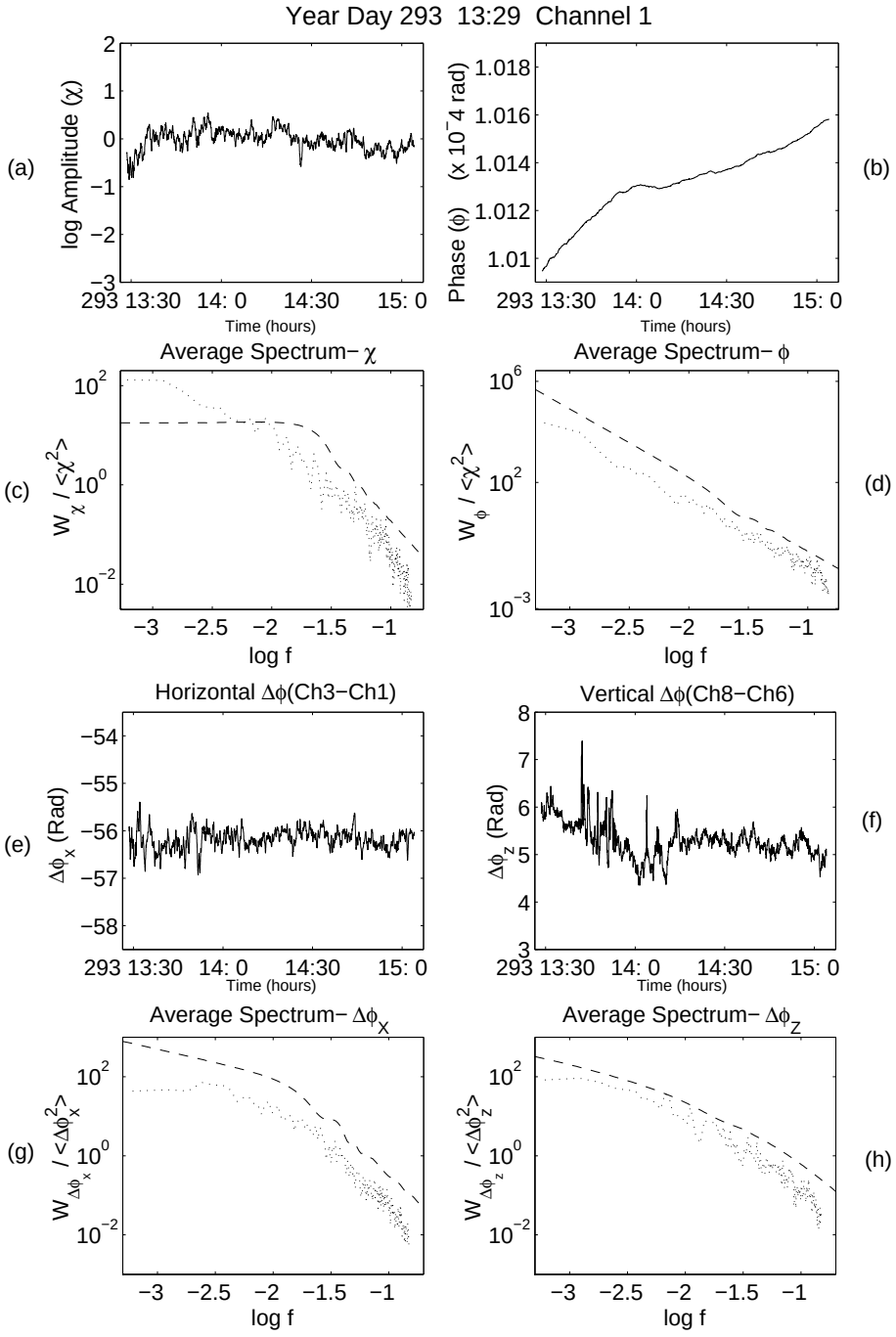

Figure 4.8: Time series of (a) log-amplitude χ and (b) phase ϕ, along with their corresponding spectra (c) and (d), respectively. (e) Horizontal phase difference $\delta\phi_x$ and (f) vertical phase difference $\delta\phi_z$, along with the corresponding normalized spectra (g) and (h), respectively. Dashed lines represent the Kolmogorov model for isotropic, homogeneous turbulence with weak scattering. The figures represent a time of low log-amplitude variance, and correspond to the diamond ($\diamond$) in Figure 4.7.

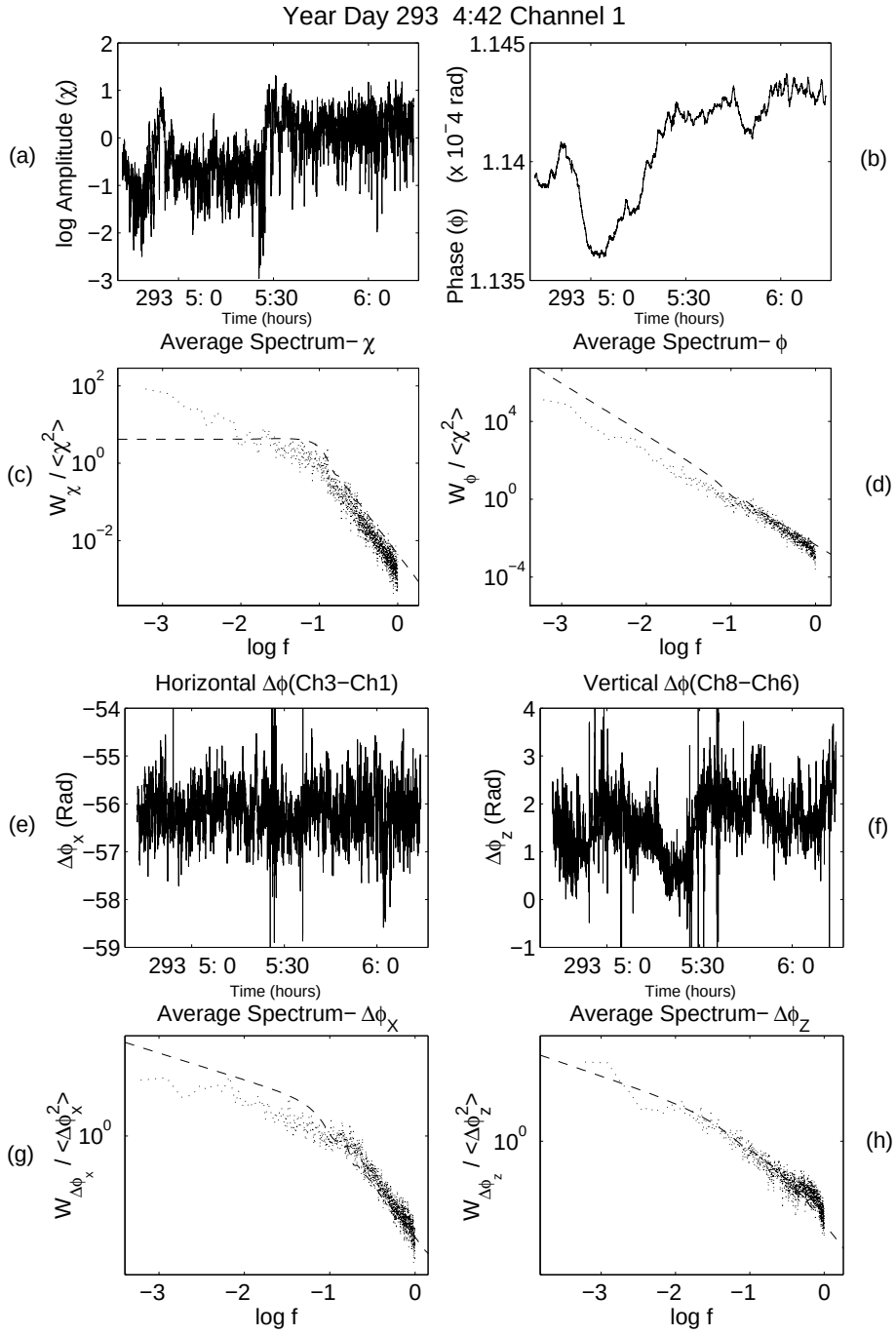

Figure 4.9: Time series of (a) log-amplitude χ and (b) phase ϕ, along with their corresponding spectra (c) and (d), respectively. (e) Horizontal phase difference $\delta\phi_x$ and (f) vertical phase difference $\delta\phi_z$, along with their corresponding normalized spectra (g) and (h), respectively. Dashed lines represent the Kolmogorov model for isotropic, homogeneous turbulence with weak scattering. The figures represent a time of when the log-amplitude variance $\sigma_\chi^2 \approx 0.25$, and correspond to the square ($\Box$) in Figure 4.7.

Chapter 5

Oceanographic Analysis

5.1 Mean Properties

5.1.1 Microcat data

Microcat pressure data is used to understand tidal dynamics during the measurement period, even though a short data set is obtained. A large sill in Admiralty Inlet, just outside of the canal entrance, dramatically influences tidal flows in and out of the channel (see Lavelle et al. (1991)), and complicates the issue of resolving the major tidal constituents. Fortunately, a large amount of historical data has been collected, including a Puget Sound circulation model maintained by NOAA/PMEL scientists at the University of Washington (refer to Lavelle et al. (1996)). Grid points in the model include a station at Foulweather Bluff, just outside of the Hood Canal entrance.

The bathymetry at the Hood Canal entrance is complex- the sill in Admiralty Inlet may dramatically alter tidal forcings, as may the steeply sloping sides of the canal entrance itself (refer to Lavelle et al. (1991)). In addition, Hood Canal is essentially closed on its southernmost end with only small river inputs (freshwater input is set to zero in recent models from Lavelle et al. (1996)), which may further complicate the tidal signal. Therefore, it is unclear whether the set of seven constituents used in the NOAA/PMEL model will accurately predict conditions at the exact site of the acoustic experiment.

Table 5.1: Frequency and relative amplitude for the four dominant tidal constituents in Hood Canal.

Tidal Constituent	Frequency (cycles/hour)	Amplitude
M2	0.08051	1.1645
K1	0.04178	0.8054
O1	0.03873	0.4010
S2	0.08333	0.3032

To clarify this issue, tidal height models were fit to the two Microcat CTD pressure records. Since the pressure records are short (≈3 days), the entire set of seven constituents used by the Puget Sound circulation model cannot be accurately resolved, and a smaller set of the four dominant constituents (defined by the PMEL model (Lavelle et al. (1996)) as M2, K1, O1, S2) was used. The Matlab harmonic analysis package t_tide, developed by Pawolwicz (2000) using Foreman (1996) Fortran software, was used to generate these models. The resulting constituent amplitudes shown in Table 5.1 are very similar to historical data from the PMEL database, and the order of relative magnitude is M2, K1, O1, S2. Figure 5.1 compares model results to the Microcat pressure data. For both moorings, the model results are very accurate, reproducing 99.2% of the variability seen in the pressure data.

5.1.2 Current meter data

Three current meters moored near the path of acoustic propagation collected data continuously throughout the acoustic experiment. These measurements are used to understand mean flows near the channel entrance, and to provide an understanding of vertical shear and stratification within the system. Current measurements were

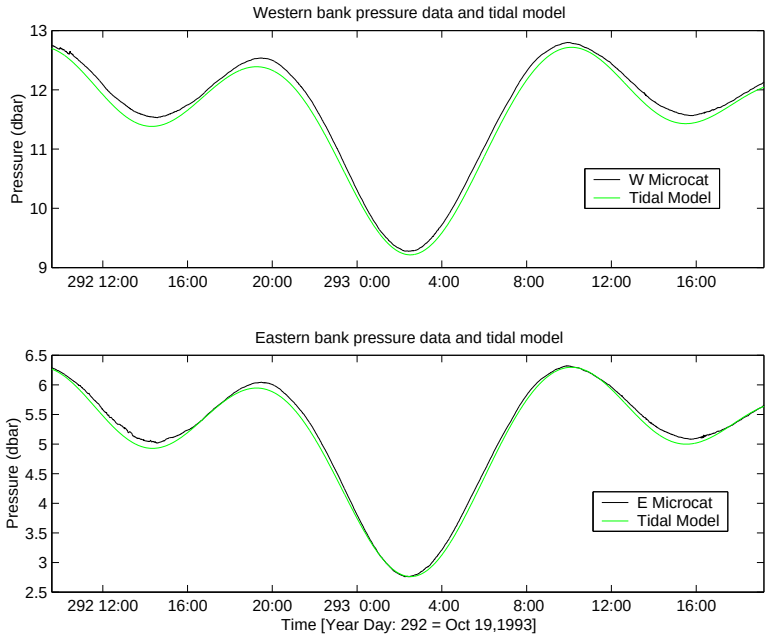

Figure 5.1: Pressure data from Microcat sensors moored on the (a) western and (b) eastern banks of the canal entrance, overlaid with the tidal model

resolved into components perpendicular and parallel to the path of acoustic propagation, which corresponds approximately to along channel ($324.25°T$ for positive ebb currents) and cross channel ($234.25°T$ for positive westward current), respectively, and are shown in Figure 5.2 (a & b).

Current parallel to the path of propagation is representative of cross-channel flow, and rarely exceeds 0.1 $\mathrm{m\,s^{-1}}$ at 40 m depth. The strongest cross-channel flows occur at 20 m depth during strong ebb events, with flows to the east at as much as $\approx 0.2\ \mathrm{m\,s^{-1}}$. These cross channel flows are presumably introduced by local bathymetric effects, including the sill in Admiralty Inlet which may impede the ebb of waters through the Hood Canal entrance (refer to Lavelle et al. (1991), analogous to the effect described by Seim and Gregg (1997)), and from possible interactions

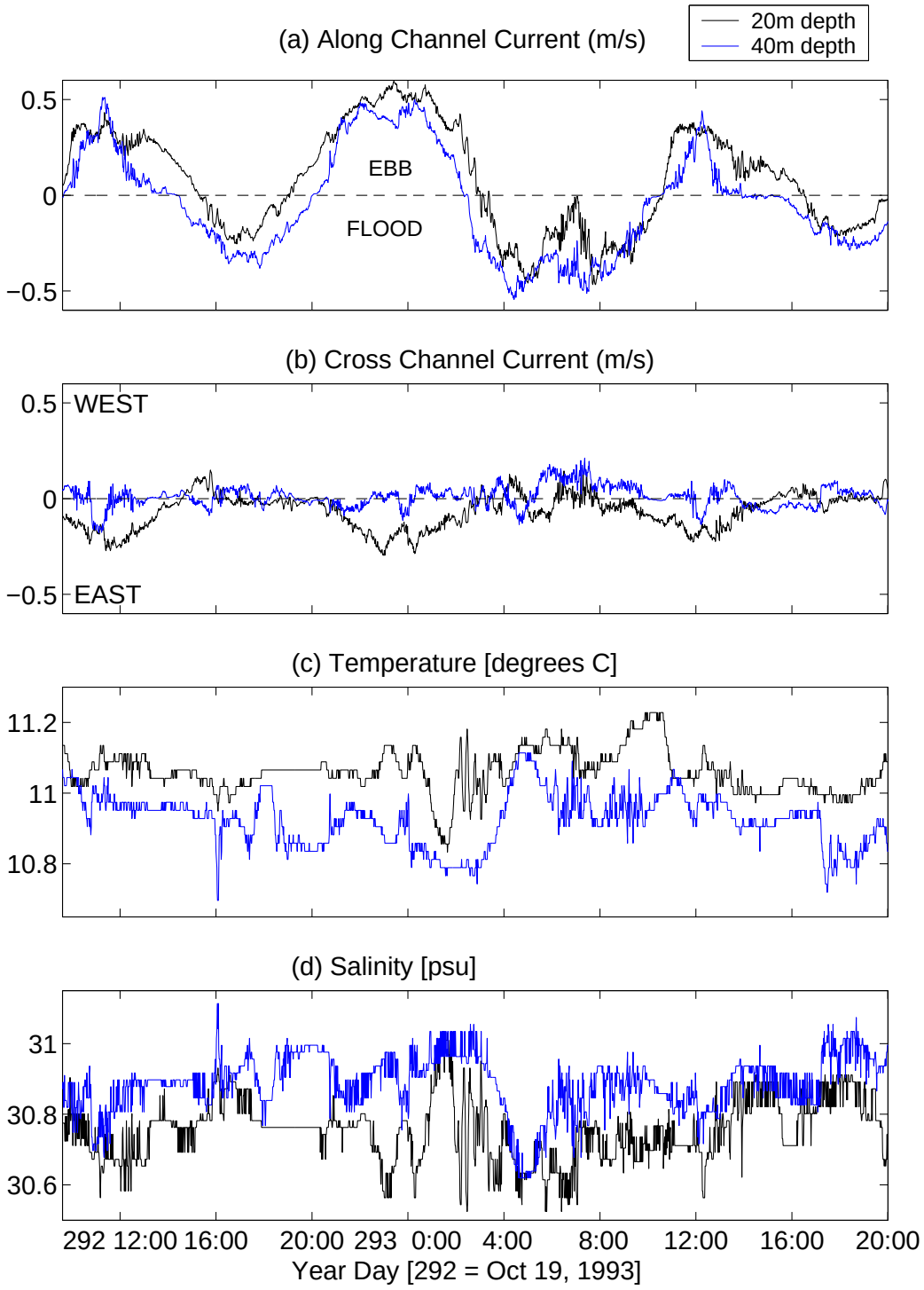

Figure 5.2: Current meter measurements at 20 m and 40 m resolved into approximately (a) along channel ($324.25°T$) and (b) cross channel ($234.25°T$) components, along with corresponding (c) temperature and (d) salinity measurements.

with the coastline anomaly known as Twin Spits (see Figure 3.1). Along-channel flows were quite strong, reaching magnitudes of up to 0.6 $\mathrm{m\,s^{-1}}$ during strong ebb and flood events. However, during the stronger of the two flood events at 6:00 AM on year day 293, current speeds are attenuated and do not reach the maximum values seen during the stronger ebb event. Since the mooring was located close to the eastern bank, both along and cross channel measurements may be influenced by the underlying bathymetry and channel curvature.

The two Aanderaa current meters also recorded temperature and salinity values at 20 m and 40 m depth, and the results are displayed in Figure 5.2 (c & d). Hood Canal is a closed channel with no significant freshwater inputs, so the salinity gradient from 20m depth to 40m depth can be expected to be small. The data shows that mean salinity values differ by 0.15psu, and mean temperature values differ by 0.15 °C.

Temperature and salinity values were also used to calculate the Brunt-Väisälä frequency (N^2), defined by Pond and Pickard (1983) as

$$N^2 = \frac{-g}{\rho}\,\frac{\partial \sigma_t}{\partial z}\ \mathrm{rad^2 s^{-2}}\ , \tag{5.1}$$

where σ_t is referenced to a depth of 20 meters for this environment, and gives a measure of the strength of stratification. The gradient is approximately $\frac{\Delta \sigma_t}{\Delta z}$ over the 20 m separation of current meters. Results across the time series are shown in Figure 5.3 (a), and for the mean temperature and salinity gradients described above, the mean Brunt-Väisälä frequency is $N^2 = 0.7 \times 10^{-4}\mathrm{rad^2 s^{-2}}$.

Figure 5.3 (b) shows the time series of current shear $\Delta U/\Delta z$ and $\Delta V/\Delta z$ for both along and cross channel flows, respectively. Together, the current shear and Brunt-Väisälä frequency provide a measure of the bulk Richardson number,

$$\mathrm{Ri} = \frac{\frac{-g}{\rho}\,\frac{\Delta \sigma_t}{\Delta z}}{(\frac{\Delta U}{\Delta z})^2 + (\frac{\Delta V}{\Delta z})^2}\ , \tag{5.2}$$

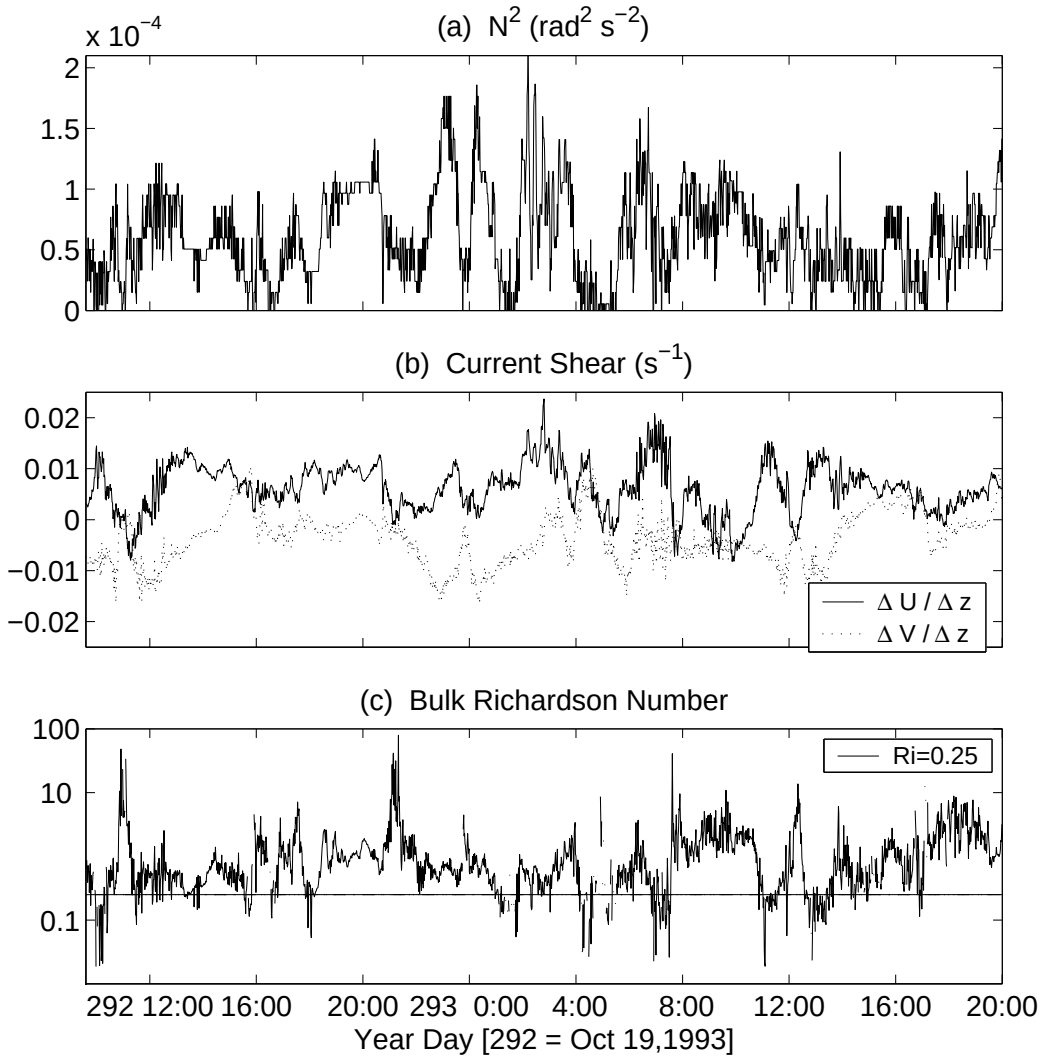

Figure 5.3: Current meter measurements of (a) Brunt-Viäsälä frequency (N^2), (b) current shear, and (c) bulk Richardson number.

and the results are shown in Figure 5.3 (c) as an indicator of water column stability. For much of the time series, Ri$>$ 0.25, and vertical stratification suppresses instabilities cause by shear. However, values of Ri frequently drop below 0.25, suggesting that shear instabilities give rise to turbulent mixing.

Comparison with tidal model

As the current meter mooring was in close proximity to the eastern boundary of the channel (see Figure 3.1), we investigate whether the current results represent mean tidal properties within Hood Canal. Current speeds at 20 m and 40 m depth are similar in magnitude, suggesting that currents in Hood Canal are dominated by the tide. From the four major tidal constituents, current models were generated using the t_tide harmonic analysis package (Pawolwicz (2000)) and compared to the vector current meter records. Using the M2, K1, S2, and O1 constituents, the current models predicted 86.6% of the measured variability at 20 m depth, and 89.4% at 40 m depth. As with the pressure models, the order of relative magnitude for the four constituents (see Table 5.2) is consistent with the historical data in the PMEL database (in Lavelle et al. (1996)), and with modelled tidal ellipses at the canal entrance (from Mofjeld (1994)). Model results are shown in Figure 5.4 (a & b) with the corresponding current meter records.

As indicated in the figure, much of the remaining variability is a result of increased cross channel flows, with resulting residual flows to the east. In the along channel direction, remaining variability arises from the current anomaly seen at 6AM on October 20. The tidal model predicts currents steadily increasing in magnitude to a maximum of 50 cm s^{-1}, while the current meter shows a sudden, marked reduction in current speed at the peak of the tidal cycle. The current meters represent a single point measurement of current, and were moored close to the eastern edge of Hood Canal. As a result, the current meter measurements may show secondary circulation

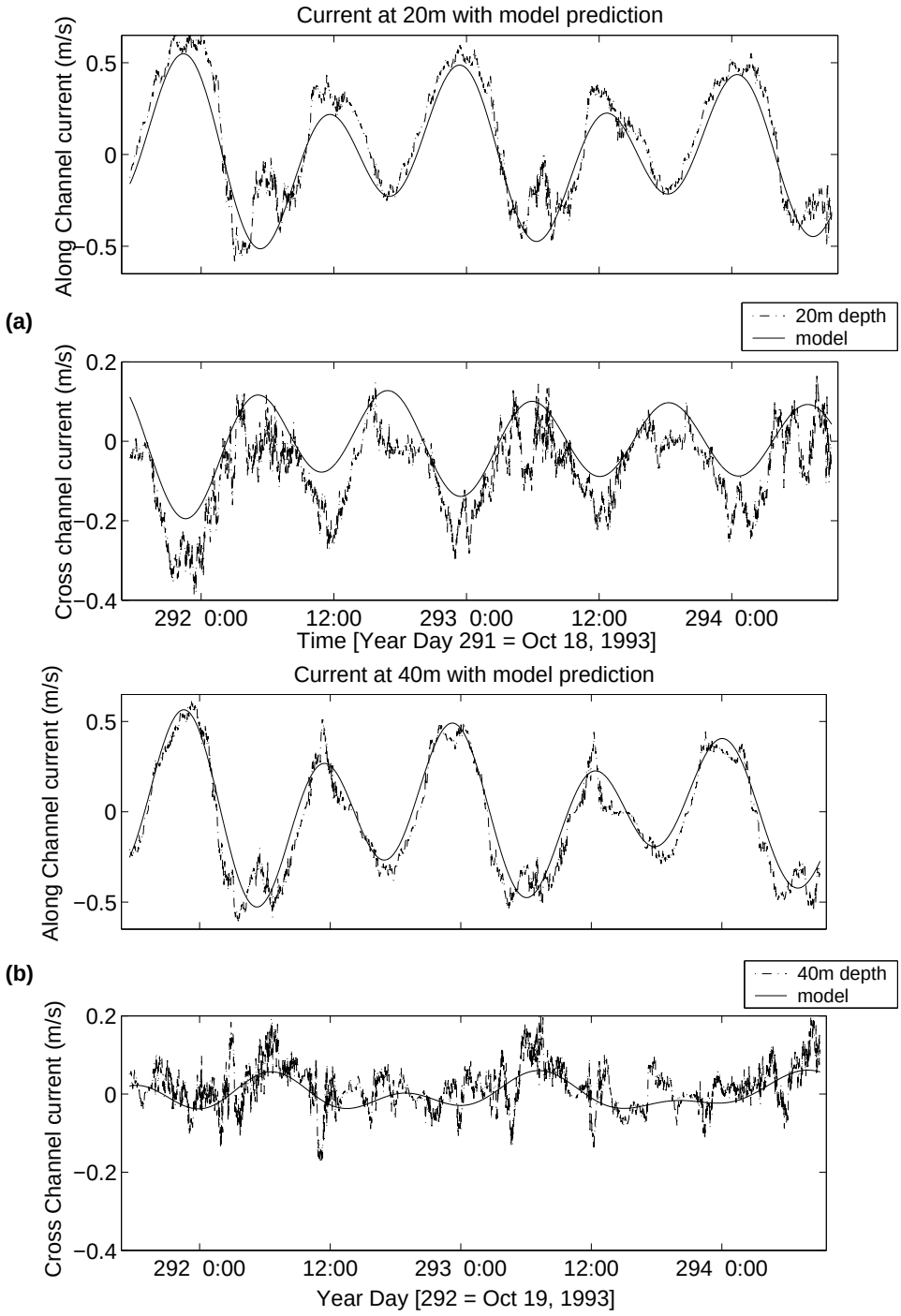

Figure 5.4: Current measurements at (a) 20 m and (b) 40 m depth, shown with the corresponding tidal models fit to vector current data.

Table 5.2: Frequency, major and minor axes, inclination, and phase for the four dominant tidal ellipses in Hood Canal at (a) 20 m depth and (b) 40 m depth.

(a)

Tidal Constituent	Frequency	Major Axis	Minor Axis	Inclination	Phase
M2	0.08051	0.452	-0.011	161.34	95.41
K1	0.04178	0.149	-0.007	149.59	58.59
O1	0.03873	0.110	-0.077	7.38	298.97
S2	0.08333	0.117	-0.016	151.54	47.86

(b)

Tidal Constituent	Frequency	Major Axis	Minor Axis	Inclination	Phase
M2	0.08051	0.379	-0.027	177.67	104.14
K1	0.04178	0.142	-0.014	167.17	79.54
O1	0.03873	0.048	0.023	22.23	293.44
S2	0.08333	0.145	-0.016	175.31	96.86

due to boundary and channel curvature effects and along and cross channel density gradients (in comparison to the results of Seim and Gregg (1997)).

5.1.3 Acoustic current calculation

Using the assumptions of isotropic, homogeneous turbulence together with the theory of weak scattering of acoustic signals, path-averaged measurements of current can be obtained from the direct path acoustic signal, since the acoustic current speed estimate is influenced by variations in the refractive index that accumulate along the path of acoustic propagation.

There are three existing methods for obtaining along channel current estimates from scintillation measurements (developed by Farmer et al. (1987)), and Di Iorio (1994) made attempts to apply each technique in previous experiments, with varying success. Scintillation current measurements obtained using the delay to the peak of

the time-lagged log amplitude cross covariance function (as will be discussed) showed best agreement with independent current measurements, and results from the other two acoustic methods were not reported in subsequent publications (see Di Iorio and Farmer (1996) and Di Iorio and Farmer (1998)). Attempts to apply each of the three methods in Hood Canal showed the same result, and therefore, only current measurements obtained from the delay to the peak method are reported herein.

The delay to the peak of the time-lagged log amplitude cross covariance function returns the time required to advect turbulent structures through the receiving array. The Taylor hypothesis assumes that these turbulent structures are statistically frozen during the time required to pass through the array, and a specific scintillation pattern is seen by each receiver as it is advected through the array. The peak of the covariance function at some time lag τ corresponds to the time separation required for a particular turbulent structure to be detected by a pair of receivers separated by r_x for parallel paths, as seen in Figure 5.5 (a), and $r_x/2$ for diverging paths, as seen in Figure 5.5 (b). For parallel acoustic paths, the along channel current estimate is simply

$$\tilde{\mathrm{U}} = \frac{r_x}{\tau}, \tag{5.3}$$

where r_x is the horizontal distance between receivers, and the $\tilde{}$ represents a path average.

Figure 5.6 shows currents calculated using the delay to the peak method for parallel paths and for the maximum receiver spacing of 3.07 meters. The time lagged covariance function is calculated using five minutes of log amplitude data, since the signals would decorrelate over longer time intervals. Therefore, the current speed measurements represent an average over five minutes. The acoustic calculations are displayed together with data from the current meter at 20 m depth and the tidal model. The acoustic results are similar to the modeled tidal currents but do not show

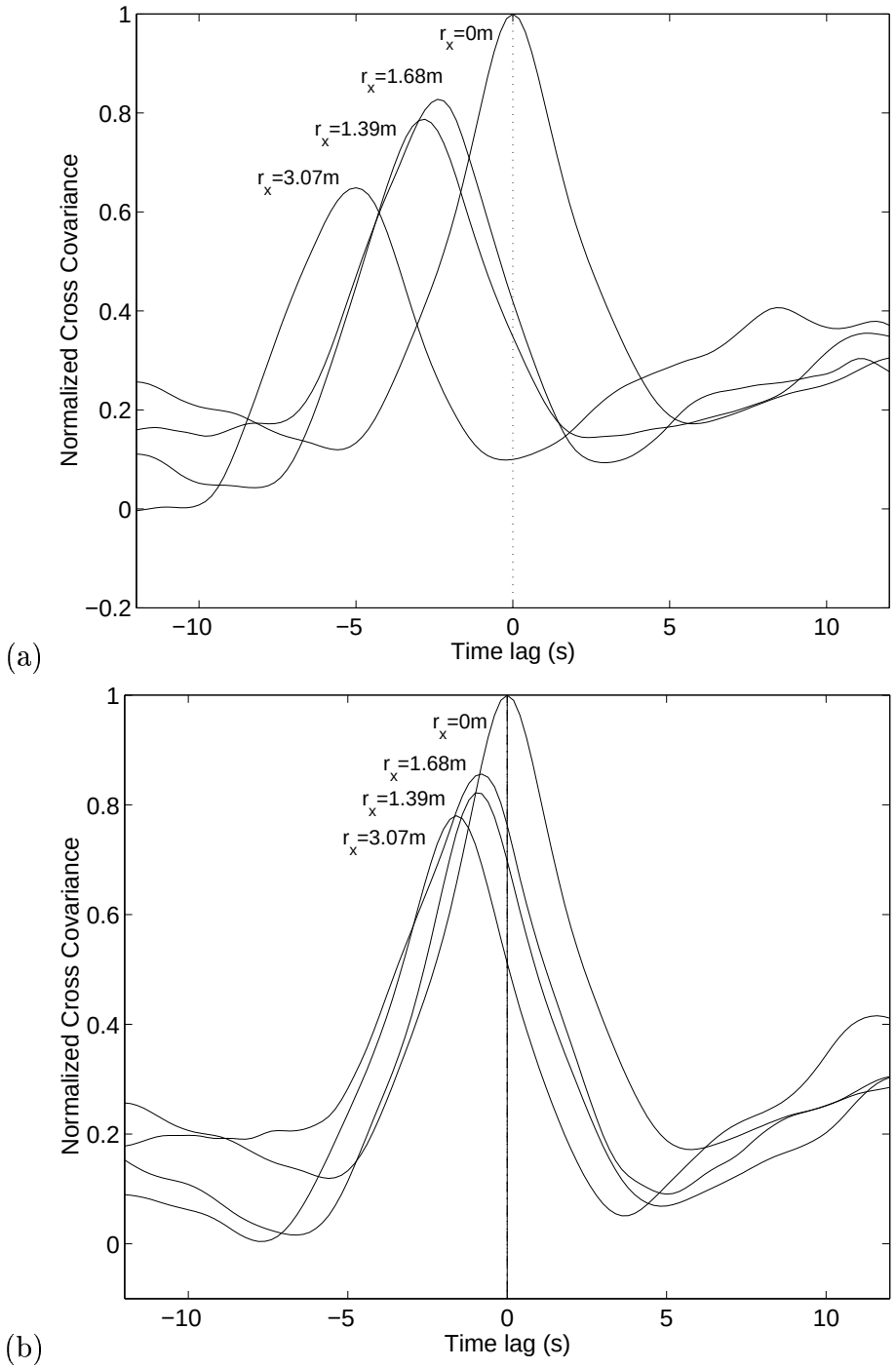

Figure 5.5: Normalized temporal cross-covariance function for log-amplitude fluctuations computed for different receiver spacings for (a) parallel and (b) diverging paths, during a time of strong tidal flow.

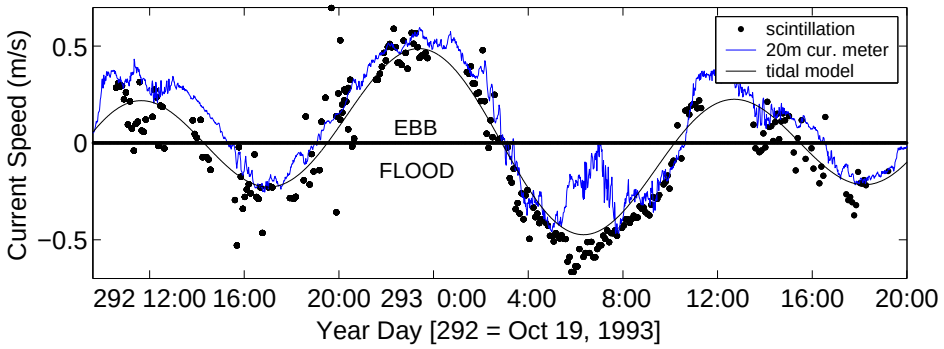

Figure 5.6: Current measurements from current meter data, scintillation measurements, and the corresponding tidal model.

the current anomaly seen in the current meter record. The scintillation measurement represents a path-averaged current measurement, with greatest weight given to mid-path effects. No current anomaly is observed, and the scintillation measurement potentially provides a spatially averaged representation of mean currents at the Hood Canal entrance.

5.1.4 Vertical arrival angle

A complete time series of sound speed measurements was generated from current meter measurements of temperature and salinity at 20 m and 40 m depth, using the MacKenzie equation (from MacKenzie (1981)). Assuming a constant sound speed gradient, the ray paths are arcs of circles (see Brekhovskikh and Lysanov (1982)). The sound speed gradient is converted to vertical arrival angle (θ_z) by

$$\tan\theta_z = \frac{L}{2c_0}\frac{dc}{dz}\,, \tag{5.4}$$

where $L = 2380$m is the path length, and the angle is measured from the horizontal axis perpendicular to the vertical CTD array. The results are shown in Figure 5.7

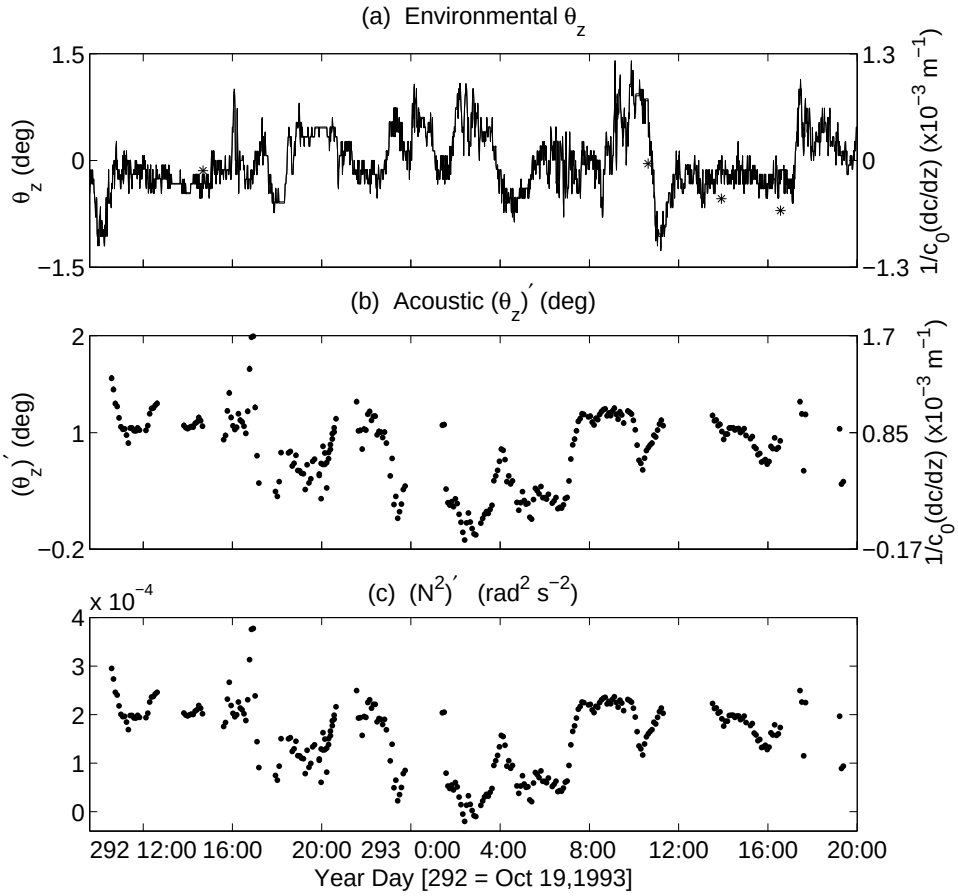

Figure 5.7: (a) Vertical arrival angle from current meter data, together with the vertical arrival angle determined from ray tracing (*), (b) acoustic vertical arrival angle fluctuations, and (c) $(N^2)'$ determined from the acoustic result.

(a), along with the vertical arrival angle determined from the ray tracing algorithm using CTD profiles denoted by (*).

The direct path acoustic measurements also provide an estimate of the vertical arrival angle of the signal. The vertical arrival angle measurement makes use of the phase difference between channels separated vertically by 1.01 meters, and is defined

by Di Iorio and Farmer (1996) as,

$$\sin\tilde{\theta}_z = \frac{(\phi_b - \phi_t)c_0}{\omega r_z} \,, \tag{5.5}$$

where the subscripts b and t are the bottom and top receivers, respectively, $\omega = 2\pi f$ is the angular acoustic frequency for $f = 67567$Hz, and the angle $\tilde{\theta}_z$ is defined relative to the horizontal line perpendicular to the vertical receiver axes. For this calculation, five minute averages of the vertical phase difference $\delta\phi_z = \phi_b - \phi_t$ are used in the conversion to a vertical arrival angle measurement. The complete time series of vertical arrival measurements in shown in Figure 5.7(b). Also shown as a second vertical axis is the sound speed gradient $(1/c_0)dc/dz$, which is obtained using the result in (5.4). The acoustic measurement also includes some undetermined angle as a result of receiver array tilt. Neglecting mean offsets, it is encouraging that orders of magnitude are comparable.

The acoustic measurement is a path integrated value, while the arrival angle obtained from the current meter represents a single point measurement. Therefore, the relative magnitudes are not expected to be identical. The two measurements are similar, however, and fluctuations about the respective mean values are comparable.

From the acoustically derived sound speed gradient, the density gradient $(1/\rho_0)\partial\rho/\partial z$ can then be approximated as follows. The sound speed gradient is determined from temperature and salinity gradients as

$$\frac{1}{c_0}\frac{\partial c}{\partial z} = a\frac{\partial T}{\partial z} + b\frac{\partial S}{\partial z} \,, \tag{5.6}$$

where $a = \frac{1}{c_0}\frac{\partial c}{\partial T}\,|_{S,P} = 2.4 \times 10^{-3}\,^{\circ}\mathrm{C}^{-1}$, $b = \frac{1}{c_0}\frac{\partial c}{\partial S}\,|_{T,P} = 8.3 \times 10^{-4}$ psu^{-1} , and the partial derivatives $\frac{\partial c}{\partial T}\,|_{S,P}$ and $\frac{\partial c}{\partial S}\,|_{T,P}$ are mean values determined from CTD data collected between 20m and 40m depth. Similarly, the density gradient can be expressed as

$$\frac{1}{\rho_0}\frac{\partial \rho}{\partial z} = \alpha\frac{\partial T}{\partial z} + \beta\frac{\partial S}{\partial z} \,, \tag{5.7}$$

where $\alpha = \frac{1}{\rho_0}\frac{\partial \rho}{\partial T} \mid_{S,P} = -1.7 \times 10^{-4}\ ^{\circ}\mathrm{C}^{-1}$ is the thermal expansion coefficient, and $\beta = \frac{1}{\rho_0}\frac{\partial \rho}{\partial S} \mid_{T,P} = 7.6 \times 10^{-4}\ \mathrm{psu}^{-1}$ is the saline contraction coefficient, which are also determined from CTD data. Assuming linear temperature/salinity diagrams with constant slope ($\frac{dT}{dS}$), the salinity gradient is expressed in terms of the temperature gradient

$$\frac{dT}{dz} = \frac{dT}{dS}\frac{dS}{dz} \,. \tag{5.8}$$

From (5.6), (5.7), and (5.8), we obtain the result for the density gradient

$$\frac{1}{\rho_0}\frac{\partial \rho}{\partial z} = \left[\frac{\alpha + \beta(\frac{\partial T}{\partial S})^{-1}}{a + b(\frac{\partial T}{\partial S})^{-1}}\right] \frac{1}{c_0}\frac{\partial c}{\partial z} \,, \tag{5.9}$$

where the term $\frac{\partial T}{\partial S}$ is determined by constructing temperature-salinity (TS) diagrams from CTD casts and measuring the mean slope defining the relationship between temperature and salinity. Finally, the density gradient is converted to Brunt–Väisälä frequency fluctuations ($(N^2)'$) by

$$(N^2)' = -g\left(\frac{1}{\rho_0}\frac{\partial \rho}{\partial z}\right) \,, \tag{5.10}$$

where $(N^2)' = N^2 - N_0^2$, and N_0^2 represents the buoyancy frequency for a medium with no refractive index variations and zero mean flow. Since the relative orientation between the transmitter and receiver arrays is unknown, we cannot determine N_o^2 exactly, and the perturbation measurement $(N^2)'$ is obtained. The complete time series of $(N^2)'$ is displayed in Figure 5.7 (c). As described for the sound speed gradient, the acoustic measurement of $(N^2)'$ is a path-averaged quantity, and therefore is not expected to be identical to the point measurement of N^2 derived from the current meters (shown in Figure 5.3). However, it is encouraging that fluctuations around some mean value are of the same magnitude. Thus, the vertical arrival angle appears to be a sensitive measure of changes in stratification at the canal entrance, as a result of path averaging.

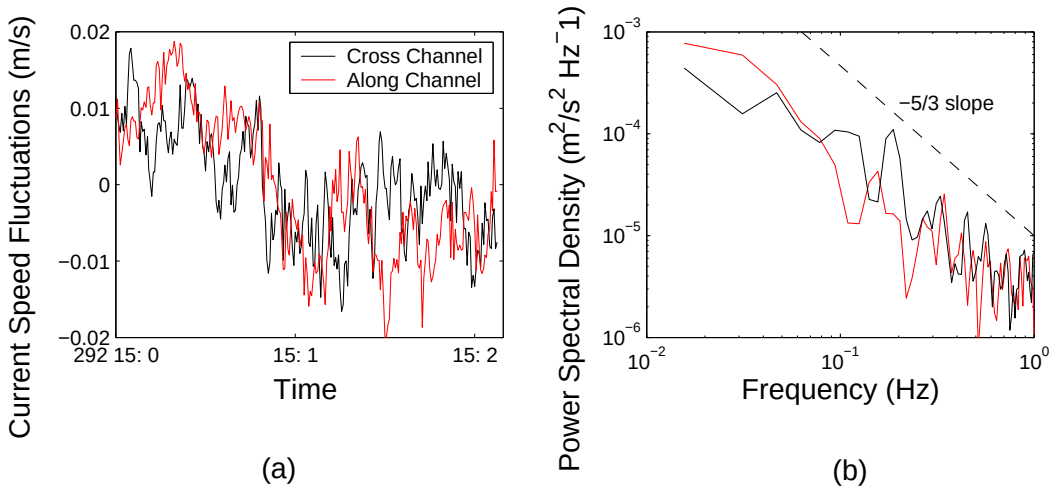

Figure 5.8: (a) Current fluctuations for a two minute burst sampled at 2 Hz, where current is resolved into approximately along channel (red) and cross channel (black) components, and the mean values have been removed, and (b) the corresponding PSDs.

5.2 Turbulent properties

Burst Sampling Current Meter

Once per hour, the burst sampling current meter at 30 meters depth collected two minutes of data, at a sampling rate of 2 Hz. Figure 5.8(a) shows current fluctuations for a single two minute burst of data, for both along and cross channel components, where the mean values have been removed. The faster sampling rate allowed estimation of the one dimensional power spectral densities (PSDs) for each current component, and the results for a single burst are shown in Figure 5.8(b). The spectrum for each component is calculated by generating eight overlapping segments of 128 data points, applying a Hanning window, fast Fourier transforming the data, and averaging over the eight spectra to obtain the one-dimensional spectrum.

For the current velocity fluctuations, the energy contained at each scale decreases with increasing frequency at $-5/3$ slope according to (2.12) and (2.13) throughout most of the experimental period, consistent with the Kolmogorov model for isotropic, homogeneous turbulence. The dashed line at $-5/3$ slope in Figure 5.8(b) is shown to support this statement, and is plotted at some arbitrary level that is not intended to represent the level of turbulent velocity fluctuations. In the cross channel spectra, there appears to be increased energy at frequency ≈ 0.2Hz. This peak in energy is presumably produced by mooring motion, and contaminates both along and cross channel spectra in several bursts of data. To remove this contamination, the frequency band $0.17 - 0.24Hz$ is omitted from the spectra in further calculations.

From the one-dimensional wavenumber spectrum shown in Equation (2.12) and making use of the Taylor hypothesis, the one-dimensional frequency spectrum for along channel velocity fluctuations is,

$$F_{11}(f) = F_{11}\left(K_1 = \frac{2\pi f}{U}\right)\frac{2\pi}{U}\,, \tag{5.11}$$

where U is the mean current speed for each burst. A similar substitution into (2.13) gives the frequency spectrum for cross channel velocity fluctuations, which should theoretically equal $4/3$ the result obtained for along channel fluctuations. On average, the measured ratio between spectra is ≈ 3.17, which suggests that the assumptions of isotropic, homogeneous turbulence are not always applicable for this stratified, tidally forced flow. However, we do expect isotropy to hold during some time within the tidal cycle, and therefore, we use the theory as a first order approximation for turbulent dissipation estimates.

Simple manipulation of (5.11) gives a result for the dissipation rate of turbulent kinetic energy (per unit mass),

$$\epsilon^{2/3} = \frac{55}{9(1.5)}F_{11}(f)f^{5/3}\left(\frac{2\pi}{U}\right)^{2/3}\,. \tag{5.12}$$

Dissipation measurements are made by averaging over the frequency band ($U/\ell_0 < f < U/\ell$) for scale sizes ℓ_0 and ℓ ranging from 1 to 10 meters, respectively. This ensures that the spectral levels are obtained within an assumed inertial subrange and out to the Fresnel scale of $\sqrt{\lambda\ell} = 7.28$ m. Also, the results will be compared to the acoustic measurement of $C^2_{n_{\rm eff}}$ in section 5.2.2 calculated from the log-amplitude variance, which is most sensitive to Fresnel scale eddies.

Figure 5.9(a) shows the time series of the dissipation measurement, where hourly measurements correspond to the calculation over each two minute burst of data. The average current for each two minute burst is shown in Figure 5.9(b) for comparison. During the strong ebb events, the dissipation rate is maximized. During the weak flood events at Year Day 292 17:00 and Year Day 293 18:00, no significant increase in dissipation is seen. However, the strong flood event at Year Day 293 6:00 produces erratic variability in ϵ, and corresponds to a time when the shear, shown in Figure 5.3(b), undergoes rapid changes.

As shown in Figure 5.9, dissipation measurements range from $\epsilon \approx 1 \times 10^{-7}\mathrm{m^2s^{-3}}$ to $\approx 1 \times 10^{-5}\mathrm{m^2s^{-3}}$ with the tidal cycle. These results are compared to the work of Seim and Gregg (1997), who obtained dissipation measurements in southern Puget Sound. Although measurements were collected in another area of Puget Sound bottom bathymetry and tidal currents were very similar. For current speeds from $0.45-0.7$ m s^{-1}, their averaged dissipation measurements ranged from $1\times10^{-6}\mathrm{m^2s^{-3}}$ to $1 \times 10^{-5}\mathrm{m^2s^{-3}}$. These results are very similar to the measurements obtained in Hood Canal with the burst sampling current meter.

The dissipation measurement, together with the measure of stratification N^2, allow estimation of a characteristic length scale for the turbulence. Stacey (1999) characterizes the Ozmidov scale,

$$L_O = (\epsilon/N^3)^{1/2} \,, \tag{5.13}$$

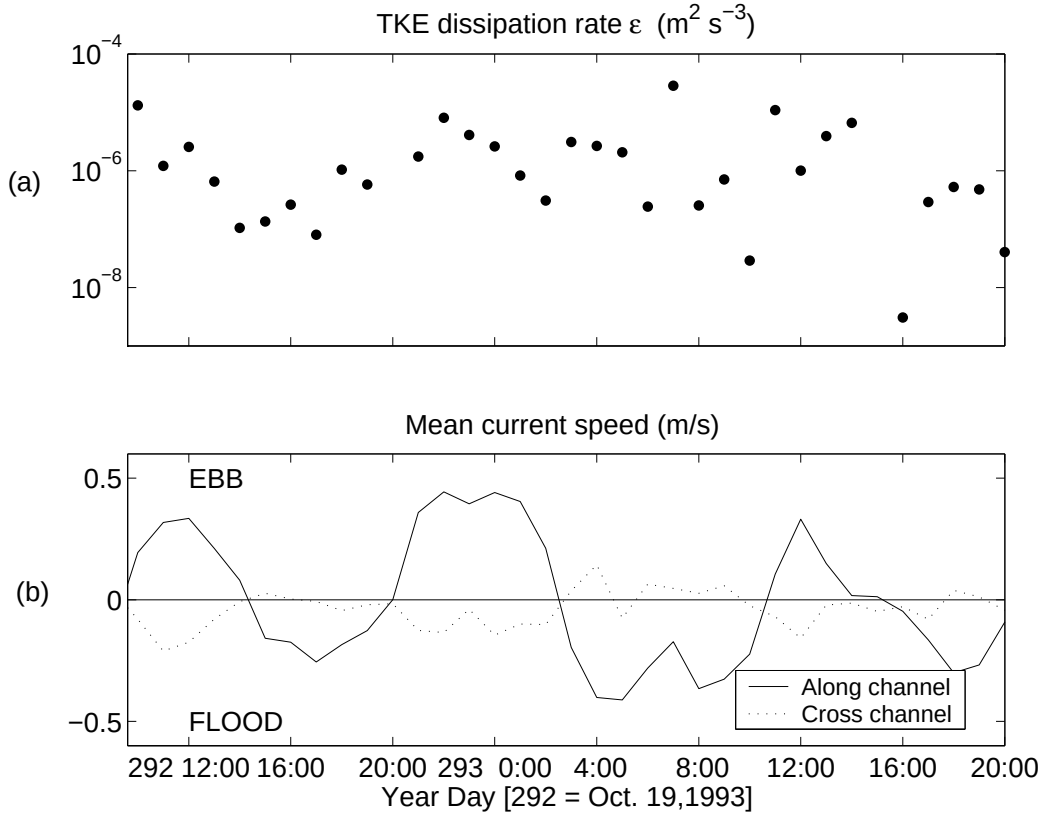

Figure 5.9: (a) Time series of the dissipation rate of turbulent kinetic energy ϵ calculated from the burst sampling current meter moored at 30 m depth, and (b) the mean along channel (solid line) and cross channel (dashed line) current speeds for each burst of data.

as the largest possible overturn that can be accomplished in the presence of stratification. For a mean dissipation of $\epsilon \approx 1 \times 10^{-6}\mathrm{m}^2\mathrm{s}^{-3}$ and a mean Brunt-Väisälä frequency of $N^2 = 0.5 \times 10^{-4}\mathrm{rad}^2\mathrm{s}^{-2}$, the burst sampling current meter gives $L_O = 1.7\ m$. This result is within the range of Ozmidov length scales observed by Stacey (1999) for turbulent flows in the presence of stratification in shallow water, where $0\,\mathrm{m} < L_O < 2\,\mathrm{m}$, and is comparable to the result $L_O = 2.8$ m obtained by Seim and Gregg (1997) for tidal flows similar to those observed in Hood Canal ($0.45\,\mathrm{m\,s}^{-1}$).

5.2.1 CTD DATA

In addition to the CTD profiles used to construct ray diagrams in section 4.1.1, two short (23 minute) time series of CTD data (sampling at 2 Hz) were also collected on Year Day 293. Temperature, salinity, and depth measurements were converted internally to sound speed measurements, and are shown in Figure 5.10 (a & b). These measurements were collected at 12 m and 30 m depth, respectively, and are shown with their corresponding PSDs in Figure 5.10 (c & d). The spectra are obtained by fast Fourier transformation of eight overlapping segments of 1024 data points with a Hanning window, and averaging to obtain the one-dimensional spectrum. Also shown in Figure 5.10 (c & d) is a line of $-5/3$ slope with arbitrary level, and comparison with the data at 30 m approximates to first order the model of isotropic, homogeneous turbulence.

The time series offers a single point in time for PSD estimation of sound speed variance levels. Using the result shown in (2.16) and invoking the Taylor hypothesis gives a result for frequency spectra, and simple manipulation gives the equation

$$C_c^2 = \frac{1}{0.124}\left(\frac{2\pi}{U}\right)^{2/3} F_c(f) f^{-5/3}, \tag{5.14}$$

where U is an average current speed evaluated at 30 m. For the sound speed spectrum at 30 m depth, the result is $C_c^2 = 3.15 \times 10^{-4}$ m$^{4/3}$s^{-2}. Inverting the result obtained in (2.9) gives

$$\epsilon_c = \frac{1}{3.82}\epsilon^{1/3} C_c^2, \tag{5.15}$$

and we obtain a measure of the dissipation rate of sound speed variance. For the average value $\epsilon = 1 \times 10^{-6}$m^{2}s^{-3} shown earlier, $\epsilon_c = 8.25 \times 10^{-7}$m^{2}s^{-3}.

5.2.2 $C_{n_{\text{eff}}}^2$ SQUARED CALCULATION

The effective refractive index fluctuations result from a combination of temperature, salinity, and current velocity fluctuations. For isotropic, homogeneous turbulence,

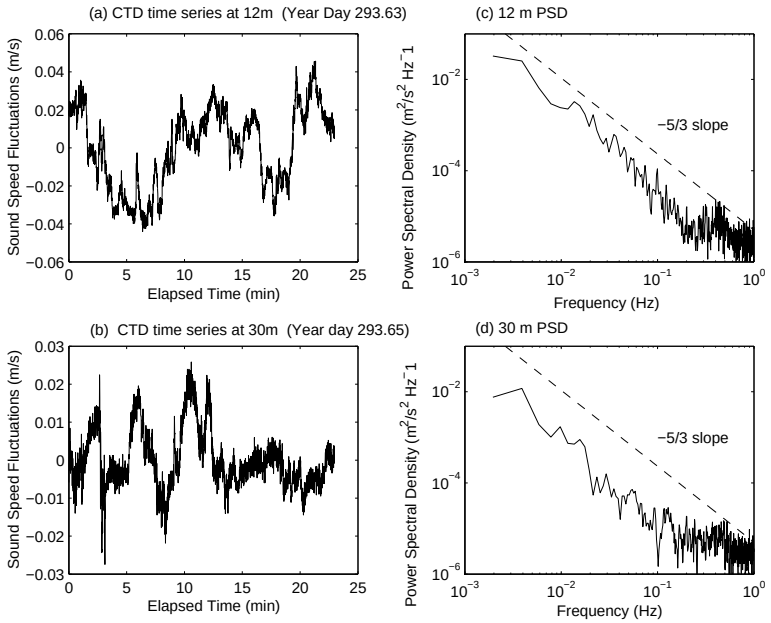

Figure 5.10: Time series of sound speed fluctuations from CTD data collected at 12 meters (a) and 30 meters (b) depth, along with the corresponding PSDs (c & d).

the structure constant $C^2_{\eta_{\text{eff}}}$ represents the level of the three-dimensional spectrum of effective refractive index fluctuations, as defined in (2.18). In a weak scattering regime ($\sigma^2_\chi \ll 0.25$) and from (2.27), the log-amplitude variance (σ^2_χ) of the acoustic signal gives an estimate of $C^2_{\eta_{\text{eff}}}$ as

$$C^2_{\eta_{\text{eff}}} = \frac{\sigma^2_\chi}{0.124} k^{-7/6} L^{-11/6}. \tag{5.16}$$

Figure 5.11(a) shows the acoustic measurement of $C^2_{\eta_{\text{eff}}}$ over a 5 minute average, which shows very high levels at times, and then reduced, stable levels at others. Some modulation with the tidal flow is evident.

The scintillation measurement of the total effective structure parameter $C^2_{\eta_{\text{eff}}}$ can be compared with the independent measurements calculated from CTD time series

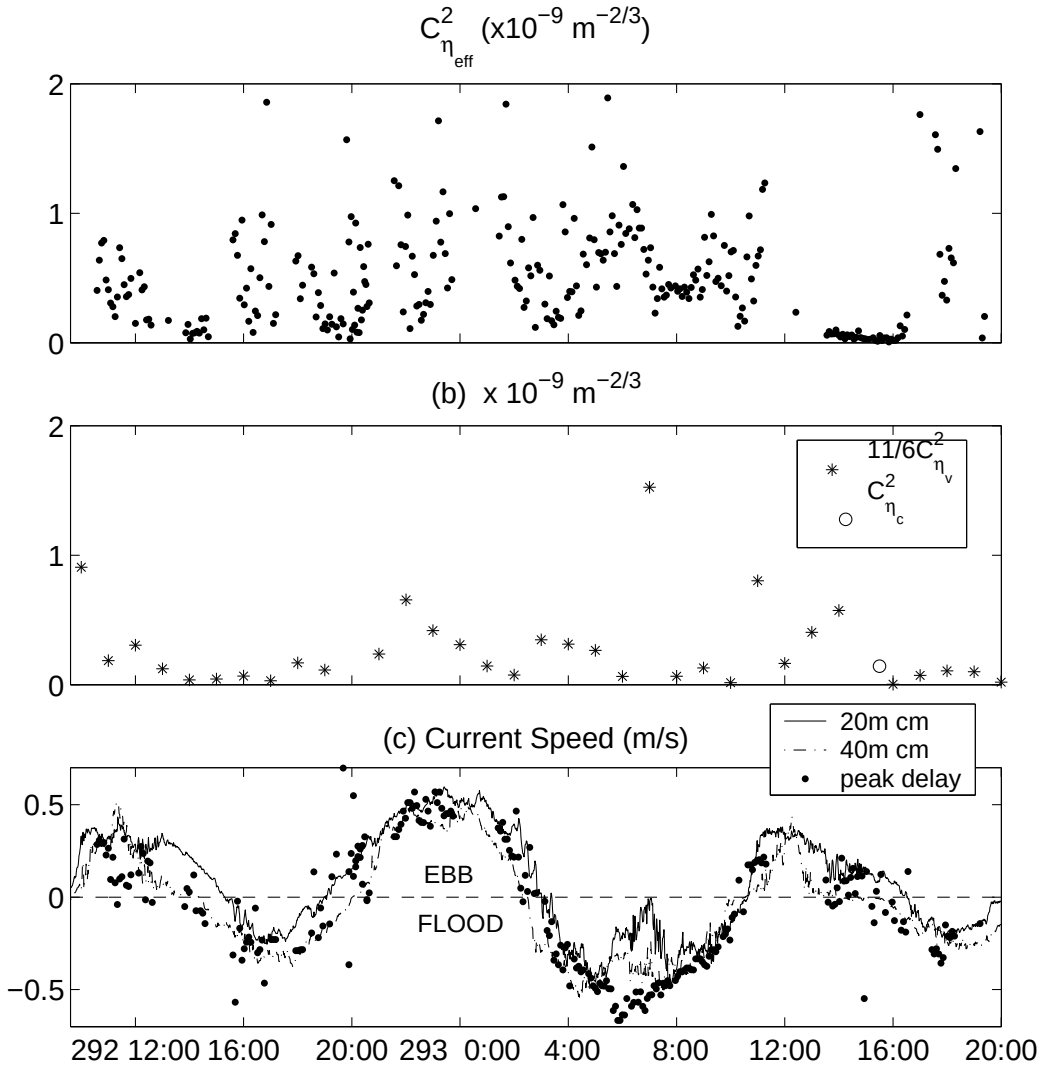

Figure 5.11: (a) Acoustically derived $C^2_{\eta_{\rm eff}}$ from log-amplitude variance, (b) $11/6\,C^2_{\eta_v}$ from burst sampling current meter along with a single measurement of $C^2_{\eta_s}$ from the CTD time series, and (c) along channel current speeds measured from the acoustics, current meter at 20 m depth, and the tidal model.

and the burst sampling current meter at 30 m depth by expressing the results as scalar and vector contributions to refractive index variability.

Scalar contributions $C_{\eta_s}^2$ to the total effective structure parameter are the result of sound speed variability, C_c^2. Dividing by the square of mean sound speed c_0^2 expresses the result as scalar contributions to refractive index variability $C_{\eta_s} = C_c^2/c_0^2$, where $c_0 = 1488$ m s^{-1} in Hood Canal. The single point measurement of refractive index variability due to scalars from the CTD time series at 30 m depth is $C_{\eta_s}^2 = 1.42 \times 10^{-10}\mathrm{m}^{-2/3}$ at Year Day 293 15:30, and the result is shown in Figure 5.11(b) as a circle. The measurement occurred near slack water, following an ebb event, and the low value suggests that well mixed water is slowly being advected past the mooring.

The dissipation rate ϵ measured from the burst sampling current meter can be converted to represent the level of velocity fluctuations C_v^2 using the relation defined in (2.6), and scaling by c_0^2 converts the result to the vector contribution to refractive index variability $C_{\eta_v}^2 = C_v^2/c_0^2$. Each hourly burst gives a single measurement of $C_{\eta_v}^2$, and the time series during the acoustic experiment is displayed in Figure 5.11 (b), plotted to the same scale as $C_{\eta_{\mathrm{eff}}}^2$.

Using the calculated value of 11/6 $C_{\eta_v}^2 = 6.52 \times 10^{-13}\mathrm{m}^{-2/3}$ at Year Day 293 16:00 with the point measurement of $C_{\eta_s}^2$ at Year Day 293 15:30 gives an estimate of the total effective structure parameter $C_{\eta_{\mathrm{eff}}}^2 = 1.44 \times 10^{-10}\mathrm{m}^{-2/3}$. The value of $C_{\eta_{\mathrm{eff}}}^2$ from the log-amplitude variance near this time is very similar, and $C_{\eta_{\mathrm{eff}}}^2 = 1.71 \times 10^{-10}\mathrm{m}^{-2/3}$ at Year Day 293 15:33. Comparison of the acoustic results to the time series of 11/6 $C_{\eta_v}^2$ shows that Hood Canal must be dominated by scalar variability through most of the tidal cycle, since the vector contribution is at most 40% of $C_{\eta_{\mathrm{eff}}}^2$, which occurs during strong ebb events. During flood events or slack water, vector contributions rarely exceed 10% of $C_{\eta_{\mathrm{eff}}}^2$, and scalar variability dominates the level of refractive index fluctuations. This represents the first application of

acoustical scintillation measurement techniques in an environment characterized by stratified, tidally forced flows where temperature/salinity variability dominates the acoustic scattering at small scales, and hence could provide an effective way to measure dissipation of scalar variance. Clear time separation of scalar and vector contributions can be carried out with reciprocal transmissions, as described by Di Iorio and Farmer (1998).

5.3 Surface characteristics

5.3.1 Meteorological data

Time series of wind speed and direction, windowed on the acoustic data, are shown in Figure 5.12, along with the corresponding air temperature and atmospheric pressure data. Winds are weak ($\approx$ 2 m s^{-1}) and from the northwest, but increase in magnitude to $\approx$ 4.5 m s^{-1} during the second day of data collection. Further analysis included in the following section will examine the surface wave field generated by these sustained winds, and explore interactions between the undulating sea surface and the near surface acoustic path.

5.3.2 Acoustics

The series of ray diagrams shown in Figure 4.2 shows temporal evolution of the near surface acoustic ray path. As discussed in Section 4.1.1, Figures 4.2(b) & (d) show near surface paths that are wholly refracted as a result of elevated surface water temperatures. The ray paths are downward-refracted in the direction of lower sound speed, and therefore do not reach the sea surface. At these times, the temporal separation between arrivals of the direct and near surface acoustic paths is small ($\approx$ 0.3ms).

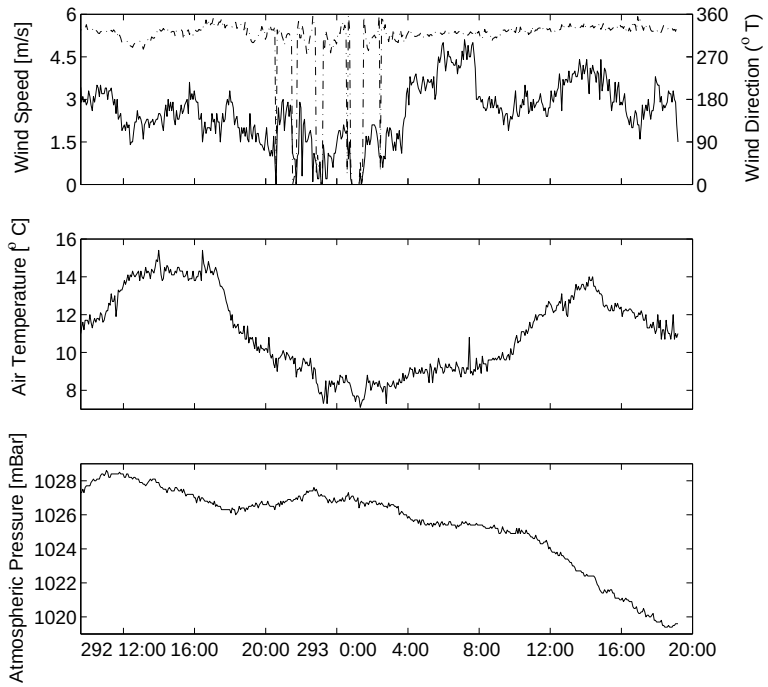

Figure 5.12: Meteorological data consisting of wind velocity at 10 m height, air temperature, and atmospheric pressure.

In Figures 4.2(a) & (c), elevated surface water temperatures are absent, and the near surface path reflects directly off the sea surface. During these events, time separation between the two acoustic arrivals arrivals is increased ($\approx$ 0.7ms), resulting from lower sound speed values in the near surface water (compared to the wholly refracted cases) and slightly longer path lengths. In the corresponding portions of the acoustic time series, increased amplitude and phase variability is observed, presumably as a result of increased acoustic scattering from surface waves and/or the orbital motions as a result of the waves (see Figure 5.13(a)).

To investigate whether or not the acoustic scintillations are indicative of surface wave features, a short (1.25 hour) time series of acoustic data was chosen,

during a time when the temporal separation between the two arrivals was rapidly evolving. From amplitude and phase measurements, the complex wave field for a given transmitter-receiver pair was calculated as

$$P(r_1, t) = A(r_1, t)e^{i\phi(r_1,t)}. \tag{5.17}$$

The resulting time series was subdivided into overlapping segments of 1024 data points and fast Fourier transformed to give power spectral density of the complex wave field. A single PSD is shown in Figure 5.13(b), for the segment of amplitude and phase time series shown in Figure 5.13(a). The spectrum shows a peak at 0.6 Hz, a frequency that may be representative of surface waves. Pierson and Moskowitz (1964) predict the peak of surface wave spectra for fully developed seas as

$$f_{max} = \frac{g}{U} f'_{max}, \tag{5.18}$$

where U is the mean wind speed, g is gravity, and f'_{max} is a constant normalized frequency. For a large range of wind speeds, they determined $f'_{max} = 0.14$, which showed little variability with changes in wind speed.

Since winds in Hood Canal are sustained from the northwest for most of the experimental period (see Figure 5.12), we make the assumption that the surface wave field is fully developed, and apply the result shown in (5.18). For the 1.25 hour time series used in this discussion, we make use of the mean wind speed $U \approx 2.5$ m s^{-1}, although wind speeds temporarily increase to ≈ 4.5 m s^{-1} during the time series. Use of the mean wind speed seems a valid approximation, since the result in (5.18) is derived for the fully developed surface wave field, which should not be significantly altered by a sudden gust of wind. Applying (5.18) gives $f_{max} \approx 0.56$ Hz, a result very similar to the spectral peak in Figure 5.13(b), which supports the assertion that the surface acoustic path is influenced by surface waves.

The time series of all PSDs calculated across the 1.25 hour interval is shown in Figure 5.14(a), along with the corresponding section of arrival time differences

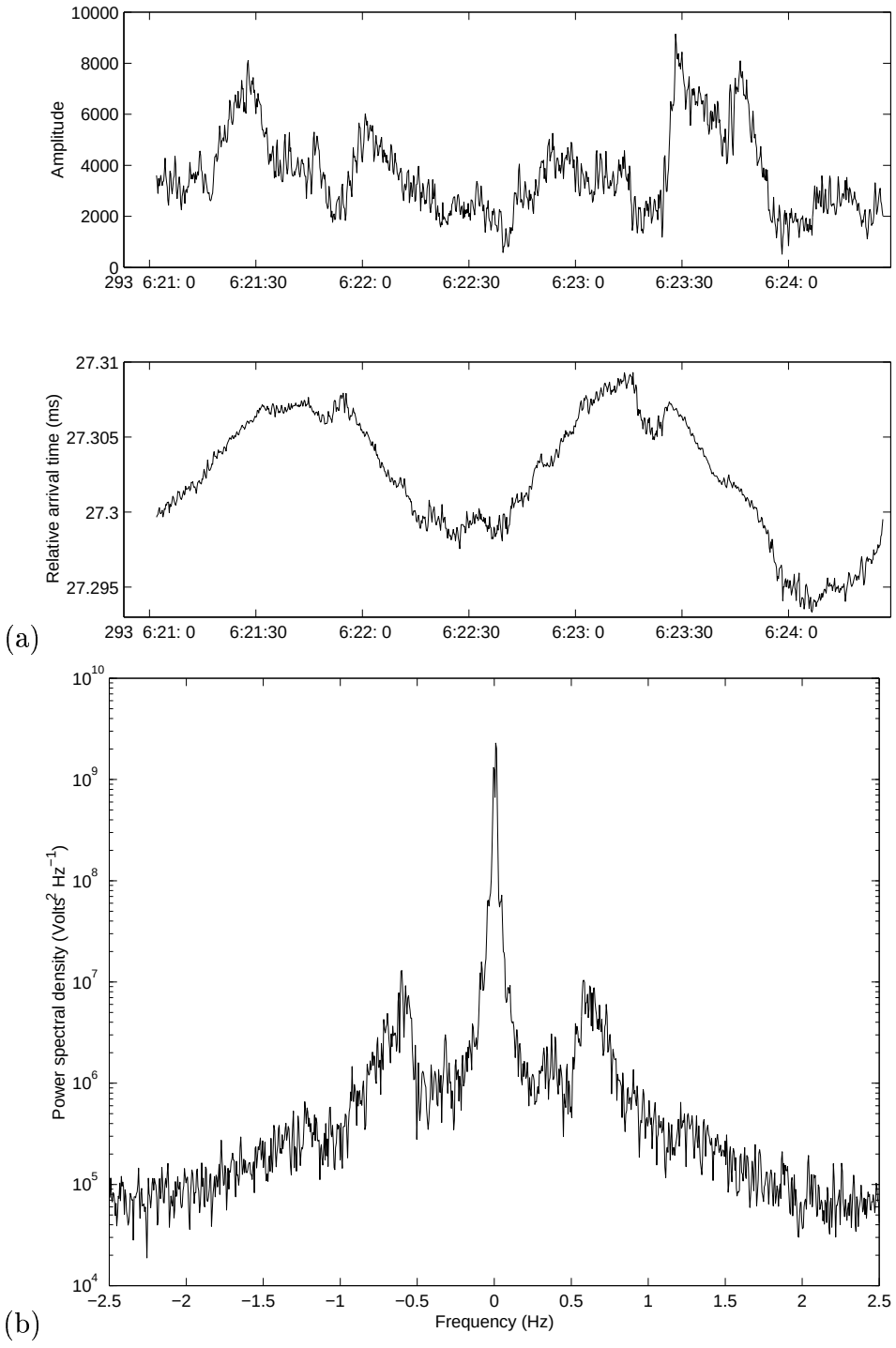

Figure 5.13: (a) Amplitude and phase (shown as relative arrival time) measurements, and (b) a sample power spectrum of the complex wave field, calculated from the approximately 3.4 minutes of amplitude and phase measurements.

between the direct and near surface acoustic paths. The arrival time difference is ≈ 0.3ms at the beginning of the time series, corresponding to a wholly-refracted near surface path. The temporal separation increases across the time series, approaching 0.7 ms at the end of time segment. The near surface path evolves to approach the sea surface, and becomes surface reflected by Year Day 293 7:42. This rapidly evolving character is also observed in the PSD time series. The intensity of the 0.6 Hz surface wave spectral peak increases across the time series, and shows the increasing effects of surface waves on the near surface acoustic path.

Calculating the spatial coherence between horizontally spaced receivers provides insight into the surface scattering process, and provides information on the direction of arrivals composing the forward scattered field. Dahl (1996) estimates the magnitude of coherence for scattering at the sea surface between two receiving elements as

$$|\Gamma(r, \tau = 0)| = \frac{|P(r_1, t)P(r_1 + d, t + \tau)^*|}{\sqrt{P^2(r_1, t)P^2(r_1 + d, t + \tau)}}, \tag{5.19}$$

where $*$ represents the complex conjugate and d is the receiver spacing. The horizontal coherence in frequency space for a receiver separation of 1.68m is shown in Figure 5.15(a), and at the 0.6 Hz surface wave peak, strong coherence is evident.

The coherence defined by (5.19) for all normalized horizontal receiver separations ($kd = 2\pi d/\lambda$, where λ is the acoustic wavelength) is shown in Figure 5.15(b), along with the horizontal coherence model developed by Dahl (1996) which is essentially related to the horizontal directivity of the received signal. Three different times are taken, corresponding to the beginning, middle, and end of the time series shown in Figure 5.14. The figure shows high coherence at all receiver spacings, although the path length (2380 m) in Hood Canal is much longer than those examined in the Dahl study, where path lengths ranged from 500-1000 meters and surface conditions were rougher. It is surprising that at this frequency and distance such high coherence

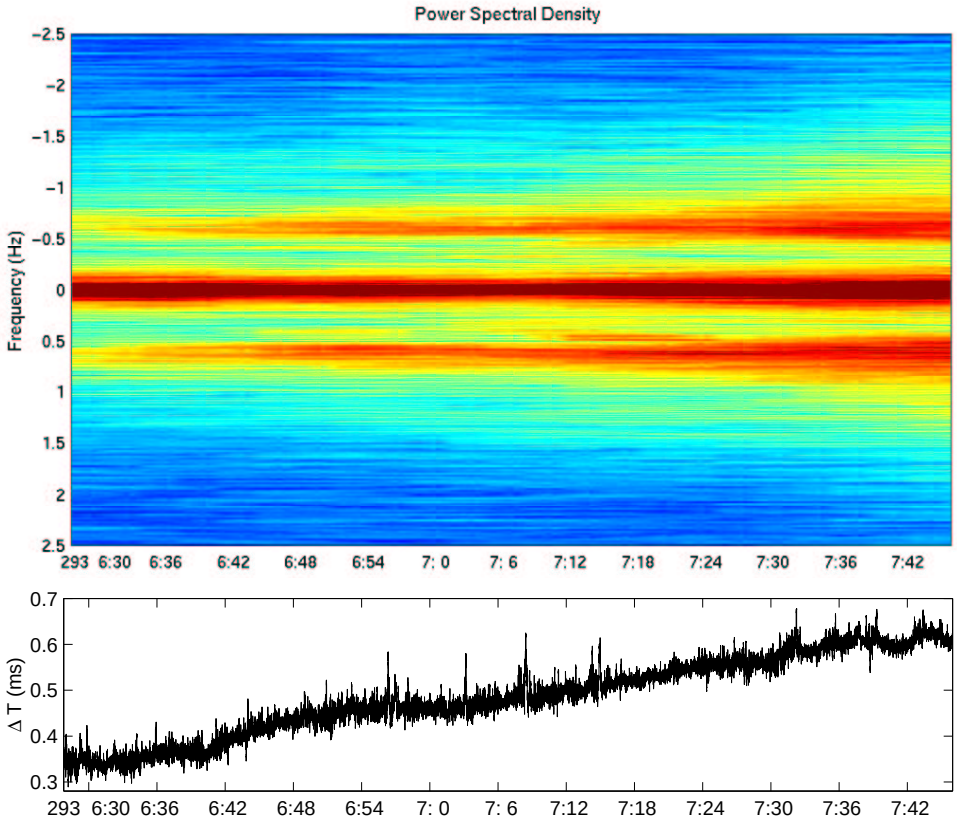

Figure 5.14: (a) Time series of power spectral densities (PSDs) of the complex wave field, with (b) the corresponding arrival time difference between the two acoustic arrivals.

is maintained. It is expected though that under more rough sea surface conditions coherence will be lost.

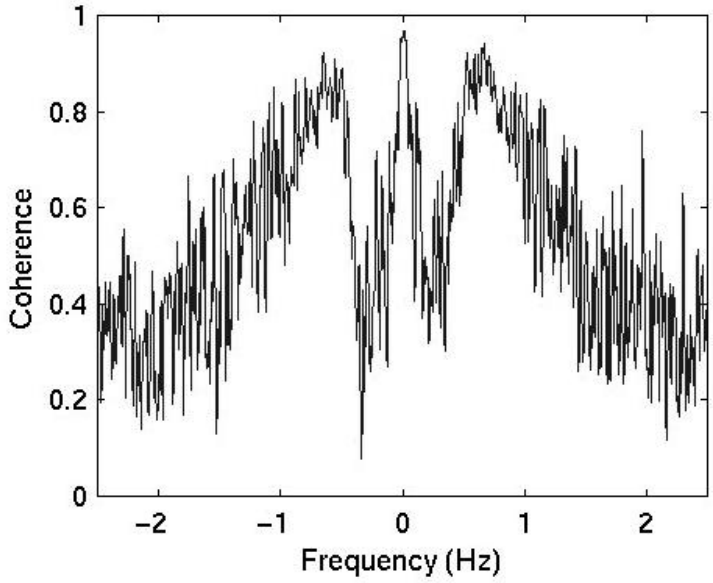

(a)

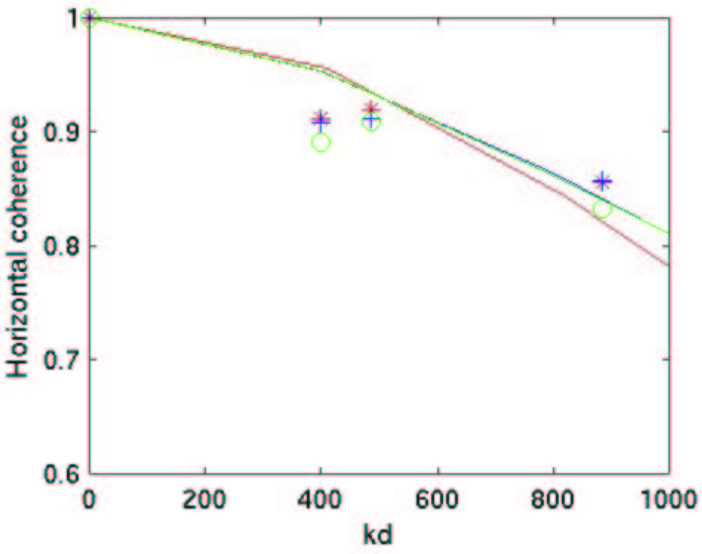

(b)

Figure 5.15: (a) Coherence for a horizontal receiver separation of 1.68m, plotted as a function of frequency, and (b) coherence for all normalized horizontal receiver separations, along with a model for horizontal coherence, taken at three different times: the beginning, middle, and end of the time series shown in Figure 5.14.

Chapter 6

Conclusion and suggestion for future work

The initial motivation for the Hood Canal Acoustic Propagation Experiment was to test the application of acoustical scintillation measurement techniques in a long range, tidally forced, stratified coastal channel. Prior experiments (see Farmer et al. (1987) and Di Iorio and Farmer (1994), for example) developed much of the theory used to apply the Kolmogorov model for isotropic and homogeneous turbulence together with the weak scattering of acoustic signals, but were limited to much shorter ranges (670 m in Cordova Channel), and in well mixed conditions. The 2380 m range in Hood Canal stretched the limitations of a 67 kHz scintillation system, and resulted in multipath arrivals throughout the experimental period. As a result, a major goal of this study was to successfully apply the maximum likelihood algorithm developed by Di Iorio and Farmer (1993) to simultaneously track and resolve precise amplitude, phase, and arrival time measurements for two closely spaced arrivals. This effort was aided by the use of a coherent transmission scheme using phase modulated PRN codes, and the two paths were successfully tracked for the majority of the experimental period.

The two-dimensional transducer arrays allowed calculation of amplitude, phase, and both horizontal and vertical phase difference spectra, which validated the use of the Kolmogorov model for isotropic, homogeneous turbulence with weak scattering at higher frequencies. The 67 kHz carrier frequency dictated that amplitude fluctuations were dominated by structures near the Fresnel radius ($\sqrt{\lambda \ell} = 7.2$ m),

and scales between 1 m and 10 m were therefore considered to dominate the turbulent measurements. Phase measurements included contributions from all scales, and scintillations in the refractive index accumulated along the propagation paths to leave a discernible pattern on both amplitude and phase measurements.

With the successful application of the Kolmogorov model with weak scattering, these scintillation patterns were used to tackle the inverse problem of deriving a number of oceanographic measurements from the direct path signal. The direct path provided a path-averaged measure of current speed, using the delay to the peak of the normalized log-amplitude cross covariance function for parallel paths. The result was compared with the current meter at 20 m depth and a tidal model generated with the four dominant tidal constituents in Hood Canal. Comparison with the tidal model was quite favorable, and currents exceeded 0.6 m s^{-1} during strong ebb and flood events. The current meter measurement was similar, except during peak flood events, when current speeds were dramatically reduced, presumably the result of some local boundary effect. This result shows the advantage of path-averaged acoustic measurements for transport calculations, which reduce the impact of local anomalies and may provide a more accurate representation of mean flows through coastal tidal channels.

Using the phase difference between vertically spaced receivers, we measured the vertical arrival angle of the signal, and applied the theoretical result to obtain a path averaged measure of the sound speed gradient. Applying mean temperature/salinity relationships from CTD data, this result was converted to Brunt-Väisälä frequency fluctuations $(N^2)'$, and provided insight into changes in stratification with the tidal cycle. To orders of magnitude, the path averaged quantity compared favorably with the current meter point measurement of mean Brunt-Väisälä frequency, where fluctuations were centered about a mean $N^2 = 0.7 \times 10^{-4} \mathrm{rad}^2 \mathrm{s}^{-2}$. This mean result, applied with the vertical shear measured from current meters at 20 m and 40 m

depth, supplied a measure of stability in terms of the Richardson number (Ri). For much of the time series, $Ri > 0.25$ and vertical stratification suppresses shear instabilities. However, Ri dropped frequently below 0.25, suggesting the current shear gives rise to turbulent mixing.

After successfully measuring these mean properties, the direct path signal was applied to understand the turbulent character of Hood Canal. The log-amplitude variance of the direct path signal provided a measure of the effective refractive index fluctuations, in terms of the effective refractive index structure parameter $C^2_{\eta_{\text{eff}}}$. Results were compared with independent measurements to understand individual vector and scalar turbulence levels.

A CTD time series provided a single measurement of scalar contributions to the turbulence, and $C^2_{\eta_s} = 1.42 \times 10^{-10} \text{m}^{-2/3}$ at Year Day 293 15:30. Near the time of the CTD time series, the vector contribution to total turbulent intensity, calculated from a fast sampling current meter at 30 m depth, gives $11/6\, C^2_{\eta_v} = 6.52 \times 10^{-13} \text{m}^{-2/3}$. Together, these measurements provide a estimate of $C^2_{\eta_{\text{eff}}} = 1.44 \times 10^{-10} \text{m}^{-2/3}$, which is compared to the acoustic result. The acoustic measurement gives $C^2_{\eta_{\text{eff}}} = 1.71 \times 10^{-10} \text{m}^{-2/3}$ at Year Day 293 15:33, a result remarkably similar to the independent estimate. The acoustic time series of $C^2_{\eta_{\text{eff}}}$ is then compared to the time series of $11/6\, C^2_{\eta_v}$ from the fast sampling current meter, and shows that scalar variability appears to dominate the turbulence in Hood Canal.

The independent measurements are also expressed in terms of more universal oceanographic quantities, and the fast sampling current meter at 30 m depth gives a complete time series of the dissipation rate of turbulent kinetic energy ϵ. On average, $\epsilon = 1 \times 10^{-6} \text{m}^2\text{s}^{-3}$. A single measurement the dissipation rate of sound speed variance is obtained from the CTD time series, and $\epsilon_c = 8.25 \times 10^{-7} \text{m}^2\text{s}^{-3}$.

Some preliminary analysis of the near surface acoustic path was also conducted. A short time series was chosen to express its temporal evolution from a wholly

refracted to surface reflected signal. Complex wave field spectra showed that surface path scintillations are dominated by surface waves, and the signals showed high spatial coherence.

6.0.3 Suggestions for future work

The major objectives of this analysis were met quite effectively, but also generated a number of ideas worthy of further consideration. Foremost in these ideas is the need to develop an acoustic array designed more specifically for long range applications. The Hood Canal experiment was a test of the theoretical limitations of scintillation measurements, and used an existing 67 kHz system designed for use over much narrower channels. Use of a lower frequency would significantly reduce multiple scatter effects in this long range environment, while allowing the user to remain focused on the turbulent scales of importance.

Although the two-path tracking algorithm worked very effectively for most of the experimental period, there were times when amplitude fade outs made it impossible to successfully track both paths. In future studies, the use of an adaptive algorithm could help to eliminate this limitation. Minimum amplitude thresholds could allow the algorithm to temporarily ignore a signal that is within the noise level, and instead window on the single dominant path. In other situations, a presence of a third stable micropath could signal the algorithm to simultaneously track $n = 3$ paths, and maximize the fit between the received and modeled signals. Perhaps concurrent evaluation for $n = 1$, $n = 2$, and $n = 3$ paths could be attempted, and the best fit to received signals could be chosen. There are, of course, many limitations inherent in creating an adaptive algorithm, due to the unstable character of intermittent micropaths. Perhaps the best solution was that mentioned earlier, to carefully select the proper acoustic frequency to reduce intermittent micropath

contamination, but the development of an adaptive algorithm remains an interesting possibility for future study.

A final suggestion is for more thorough investigation of the near surface acoustic path. This signal showed high spatial coherence in Hood Canal, which may have important implications for applications in coastal acoustic communication. These coherence measurements have been parameterized by Dahl (1996) in earlier experiments to produce coherence models influenced by sea surface slope, swell, and small surface waves. It is surprising that a high level of coherence is obtained over this long path length and over a large receiver aperture of 3.07 m, and warrants further investigation.

Bibliography

Alford, M., M.C.Gregg, and Ilyas, M. (1999). Diapycnal mixing in the banda sea: Results of the first microstructure measurements in indonesian throughflow. *Geophysical Research Letters*, 26 (17):2741–2744.

Baggeroer, A. B., Birdsall, T. G., Clark, C., Colosi, J. A., Cornuelle, B. D., Costa, D., Dushaw, B. D., Dzieciuch, M., Forbes, A. M. G., Hill, C., Howe, B. M., Marshall, J., Menemenlis, D., Mercer, J. A., Metzger, K., Munk, W., Spindel, R. C., Stammer, D., Worcester, P. F., , and Wunsch., C. (1998). Ocean climate change: Comparison of acoustic tomography, satellite altimetry, and modeling. *Science*, 281:1327–1332.

Bjerrum-Niese, C. (1998). *Influence of the dynamic sea surface on underwater acoustic communication.* PhD dissertation, Technical University of Denmark.

Bowlin, J. (1994). Ray tracing algorithm 'ray' version 1.47. Woods Hole Oceanographic Institution.

Brekhovskikh, L. and Lysanov, Y. (1982). In Ecker, G., Engl, W., and Felsen, L. B., editors, *Fundamentals of Ocean Acoustics*, number 8 in Springer Series in Electrophysics. Springer-Verlag, Berlin.

Chernov, L. (1960). *Wave Propagation in a Random Media.* Translated from Russian by R. A. Silverman, McGraw-Hill Inc.

Clifford, S. (1971). Temporal-frequency spectra for a spherical wave propagating through atmospheric turbulence. *Journal of the Optical Society of America*, 61:1285–1292.

Clifford, S. and Farmer, D. (1983). Ocean flow measurements using acoustic scintillation. *Journal of the Acoustical Society of America*, 74 (6):1826–1832.

Colosi, J. (1996). Mode coupling by internal waves for multimegameter acoustic propagation in the ocean. *Journal of the Acoustical Society of America*, 100 (6):3607–3620.

Dahl, P. (1996). On the spatial coherence and angular spreading of sound forward scattered from the sea surface: Measurements and interpretive model. *Journal of the Acoustical Society of America*, 100 (2):748–758.

Di Iorio, D. (1994). *Measurements of Turbulence Parameters and Observations of Multipath Arrivals in Two Contrasting Coastal Environments Using Acoustical Scintillation Analysis*. PhD dissertation, University of Victoria.

Di Iorio, D. and Farmer, D. (1993). Observations of acoustical scintillations in Saanich Inlet. In *IEEE Oceans '93 Proceedings*, October 18-21, Victoria, B.C. Canada.

Di Iorio, D. and Farmer, D. (1994). Path-averaged turbulent dissipation measurements using high-frequency acoustical scintillation analysis. *Journal of the Acoustical Society of America*, 96:1056–1069.

Di Iorio, D. and Farmer, D. (1996). Two-dimensional angle of arrival fluctuations. *Journal of the Acoustical Society of America*, 100:814–824.

Di Iorio, D. and Farmer, D. (1998). Separation of current and sound speed in the effective refractive index for a turbulent environment using reciprocal acoustic transmission. *Journal of the Acoustical Society of America*, 103:321–329.

Ehrenberg, J., Ewart, T., and Morris, R. (1978). Signal processing techniques for resolving individual pulses in a multipath signal. *Journal of the Acoustical Society of America*, 63 (6):1861–1865.

Farmer, D. and Clifford, S. (1986). Space-time acoustic scintillation analysis: A new technique for probing ocean flows. *IEEE Journal of Oceanic Engineering*, OE-11:42–50.

Farmer, D., Clifford, S., and Verrall, J. (1987). Scintillation structure of a turbulent tidal flow. *Journal of Geophysical Research*, 92:5369–5382.

Farmer, D. and Crawford, G. (1991). Remote sensing of ocean flows by spatial filtering of acoustic scintillations: Observations. *Journal of the Acoustical Society of America*, 90:1582–1591.

Fleury, M. and Lueck, R. (1992). Microstructure in and around a double-diffusive interface. *Journal of Physical Oceanography*, 22 (7):701–718.

Foreman, M. (1979-1996). Manual for tidal currents analysis and prediction. Technical report, Institute of Ocean Sciences, Patricia Bay Sidney, British Columbia.

Gustafson, R., Lenarz, W., McCain, B., Schmitt, C., Grant, W., Builder, T., and Methot, R. (2000). Status review of pacific hake, pacific cod, and walleye pollock from puget sound, washington. Technical report, NOAA Technical Memorandum NMFS-NWFSC-44.

Henyey, F., Wright, J., and Flatte, S. (1986). Energy and action flow through the internal wave field: An eikonal approach. *Journal of Geophysical Research*, 91:8487–8596.

Hinze, J. O. (1959). *Turbulence: An Introduction to its Mechanism and Theory.* McGraw-Hill Series in Mechanical Engineering.

Ishimaru, A. (1978). *Wave Propagation and Scattering in Random Media, Vol. 2.* Academic Press, Inc.

Lavelle, J., Cokelet, E., and Cannon, G. (1991). A model of density intrusions into and circulation within a deep, silled estuary: Puget sound. *Journal of Geophysical Research*, 96 (C9):16779–16800.

Lavelle, J., Mofjeld, H., Lempriere-Doggett, E., Cannon, G., Pashinski, D., Cokelet, E., Lytle, L., and Gill, S. (1979-1996). A multiply-connected channel model of tides and tidal currents in puget sound, washington and a comparison with updated observations. Technical report, NOAA Technical Memorandum ERL PMEL-84.

Lemon, D., Knight, D., Chave, A., and Farmer, D. (1987). An acoustic system for measuring ocean flows by space-time scintillation analysis. In *IEEE Oceans '87 Proceedings,*, September 28-October 1, Halifax, Nova Scotia, Canada.

MacKenzie, K. (1981). Nine term equation for sound speed in the ocean. *Journal of the Acoustical Society of America*, 70:807–812.

Menemenlis, D. and Farmer, D. (1992). Acoustical measurements of current and vorticity beneath ice. *Journal of Atmospheric and Oceanic Technology*, 9(6):827–849.

Mofjeld, H. (1994). Hood canal tidal ellipses (personal communication). School of Oceanography, University of Washington.

Munk, W. (1981). A survey of internal waves and small-scale processes. In Warren, B. and Wunch, C., editors, *Evolution of Physical Oceanography*. Cambridge, MA: MIT Press.

Ostachev, V. (1994). Sound propagation and scattering in media with random inhomogeneities of sound speed, density, and medium velocity. *Waves in Random Media*, 1:1–26.

Ostachev, V. (1997). *Acoustics in Moving Inhomogeneous Media*. Thompson Science and Professional.

Pawolwicz, R. (2000). Matlab harmonic analysis package 't_tide.m'. Department of Earth and Ocean Sciences, University of British Columbia.

Pierson, W. and Moskowitz, L. (1964). A proposed spectral form for fully developed wind seas based on the similarity theory of s.a. kitaigorodskii. *Journal of Geophysical Research*, 69 (24):5181–5190.

Pond, S. and Pickard, G. (1983). *Introductory Dynamical Oceanography*. Pergamon Press, 2nd edition.

Press, W. H., Teukolsky, S. A., Vetterling, W. T., and Flannery, B. P. (1992). *Numerical Recipes in C: The Art of Scientific Computing, 2nd edition*. Cambridge University Press.

Seim, H. and Gregg, M. (1997). The importance of aspiration and channel curvature in producing strong vertical mixing over a sill. *Journal of Geophysical Research*, 102 (C2):3451–3472.

Shaw, W., Trowbridge, J., and III, A. W. (2001). Budgets of turbulent kinetic energy and scalar variance in the continental shelf bottom boundary layer. *Journal of Geophysical Research*, 106 (C5):9551–9563.

Stacey, M. T. (1999). Observations of turbulence in a partially stratified estuary. *Journal of Physical Oceanography*, 29:1950–1970.

Tatarskii, V. (1961). *Wave Propagation in a Turbulent Medium*. McGraw-Hill, New York.

Tatarskii, V. (1971). *The Effects of the Turbulent Atmosphere on Wave Propagation*. Translated from Russian by Israel Program for Scientific Translations, Jerusalem.

Tennekes, H. and Lumley, J. (1999). *A First Course in Turbulence*. MIT Press.